Rochester Institute of Technology

RIT Digital Institutional Repository

2005

Integration of micromachined thermal thermal shear stress sensors with microchannels - design, fabrication and testing

Vinod Dilip Kulkarni

Follow this and additional works at: https://repository.rit.edu/theses

INTEGRATION OF MICROMACHINED THERMAL SHEAR STRESS SENSORS WITH MICROCHANNELS – DESIGN, FABRICATION AND TESTING

by

Vinod Dilip Kulkarni

A Thesis submitted in

Partial Fulfillment of the

Requirement for the degree of

MASTER OF SCIENCE

IN

MICROELECTRONIC ENGINEERING

Approved by:

Dr. Risa Robinson   _____

Department of Mechanical Engineering   (Thesis Advisor)

Dr. Lynn Fuller   _____

Department of Microelectronic Engineering   (Thesis Advisor)

Dr. Karl Hirschman   _____

Department of Microelectronic Engineering   (Committee Member)

Dr. Santosh Kurinec   _____

Department Head of Microelectronic Engineering

DEPARTMENT OF MICROELECTRONIC ENGINEERING

ROCHESTER INSTITUTE OF TECHNOLOGY

PERMISSION GRANTED

Title of thesis:

INTEGRATION OF MICROMACHINED THERMAL SHEAR STRESS SENSORS WITH MICROCHANNELS –DESIGN, FABRICATION AND TESTING

I, Vinod Dilip Kulkarni, hereby grant permission to the Wallace Library of the Rochester

Institute of Technology to reproduce my thesis in whole or in part. Any reproduction will

not be for commercial use or profit.

Date:_____   Signature of Author:_____

A tribute of love to my parents,

Dilip and Rajani

for their love, encouragements,

blessings and support

Acknowledgements

Abstract

The emerging picture of microvascular flow strongly suggests that local gradients in shear rate along the arteriole walls play an integral role in the ability of a microvascular network to regulate and modify blood flow. The methods to estimate shear stress from approximations of the velocity profiles determined by in vivo particle tracking experiments in the hamster and computational simulation are limited by assumptions made about the flow and experimental techniques (Noren, 1999). Right now, our ability to relate wall shear stress in microvessels to corresponding biological function is limited by our ability to accurately determine shear stress. A three dimensional computational model was created to simulate the system's thermal response to the constant temperature control circuit. The model geometry included all fabricated layers in thermal shear stress sensor and the microchannel structure (17 μm x 17 μm). This computational technique was used to optimize the dimensions of the system in order to reduce the amount of heat lost to the substrate and maximize the signal response. Hot film thermal shear stress sensors were successfully integrated with microchannel using surface micromachining technique. The entire device was fabricated and tested at Semiconductor Microsystems Fabrication Laboratory (SMFL) at RIT. This thesis discusses the design and optimization of a thermal shear stress sensor using computational techniques to simulate the sensor's performance in microchannel models of arteriole bifurcations. An attempt has been made to verify thermal-transfer principle of hot film shear stress sensors in microchannels.

Table of Contents

List of Figures

List of Tables

Chapter 1

Introduction

1.1 Background

The human microcirculation system is responsible for transport of oxygen carrying red blood cells (RBCs), activation of white blood cells, and transport of chemical messengers. The oxygenated blood from the heart flows into the arteries which are responsible for carrying blood to capillary networks and branch into bifurcations of divergent flows. A healthy tissue metabolism depends upon the abundant oxygen supply from the blood flow in the microcirculation system in body. RBCs [erythrocytes] contain oxygen molecules and supply them to tissues in the capillary network. Endothelial cells (50-100 μm in length) line the inner surface of the arterioles as large curved plates. These cells respond to the stimulation by chemical messengers, signals conducted from

neighboring cells, and fluid shear forces (Noren, 1999). Endothelial cells sense shear rate gradients and respond to these changes by producing vasoactive agents. Some of these agents cause immediate dilation or constriction and divert the flow within the vascular network. Other agents cause long term changes in new blood vessel growth (angiogenesis) which are required for wound healing, or lead to loss of blood vessels (rarefaction) which is common in diabetes. Thus, from these responses of endothelial cells to shear stress, one can conclude that the shear stress distribution in arteriolar bifurcations plays an integral role in blood flow regulation (Robinson et al., 2003). The present limitation is to accurately determine wall shear stress in microvessels and relate this stress to the corresponding biological function or response. The objective of this thesis was to build an *in vitro* model of *in vivo* blood flow circulation system using a silicon micromachining technology. By using water as a working fluid and integrating microchannels ($17*17$ μm^2) with bifurcation angles 30^0 with micromachined thermal shear stress sensors, an attempt has been made to investigate the value of the wall shear stress.

1.2 MEMS

Micro-Electro-Mechanical Systems (MEMS) is the integration of mechanical elements, sensors, actuators, and electronics on a common silicon substrate through the utilization of microfabrication technology. While the electronics are fabricated using integrated circuit (IC) process sequences (e.g., CMOS, Bipolar, or BICMOS processes), the micromechanical components are fabricated using compatible micromachining processes that selectively etch away parts of the silicon wafer or add new structural layers to form the mechanical and electromechanical devices.

Microelectromechanical systems (MEMS) have received great deal of attention because of increased miniaturization and performance of MEMS devices over conventional devices. Microelectromechanical systems (MEMS) are poised to capture a large segment of the sensor market.

One of the major advantages of the MEMS devices (Liu, 1996) is the small size. The dimension of MEMS devices range form 1 µm to 1 mm. Due to small sizes less real estate is needed and mechanical, electrical and thermal response times are much smaller compared to those of macro-devices. Some scaling rules of physical characteristics are illustrated below (Trimmer, 1989 and Madou, 1997).

Consider, S = multiplicative scaling factor i.e. the new size of the system will be the original dimension multiplied by 'S'. Assuming that all three spatial dimensions scale identically (Isomorphically), Table 1-1 gives a partial list of scaling behavior.

Table 1-1 Micro-world scaling behavior

QUANTITY	SCALING
Mass Density	S^0
Pressure	S^0
Viscosity	S^0
Area	S^2
Mass	S^3
Volume	S^3
Number of Particles	S^3

Thus, the surface effects (e.g. stiction and friction) will be of importance in the micro world whereas volume effects (e.g. gravitation and inertia) will be relatively more important in the macro world. In summary, some of the implications of small size are that inertial forces become insignificant while viscous forces and friction dominate. Isolation

from the universe becomes easily achievable. Virtually all fluid flows are laminar and the surface effects dominate over bulk effects.

The other major advantage of MEMS devices is the leveraging from existing IC industry and batch manufacturability. Many of the manufacturing processes and tools from the integrated circuit industry such as photolithography, oxidation and diffusion, wet cleaning and etching, thin film deposition, ion implantation can be used for the fabrication of MEMS. Due to this leveraging from a large industrial base, the development cost is reduced for MEMS devices. IC fabrication is a batch process in which hundreds to thousands of units are simultaneously created on a single wafer. Hence the result is production in large volume with low unit cost.

1.3 Silicon Microfabrication Techniques

Silicon microfabrication techniques are mainly categorized as bulk micromachining and surface micromachining (Madou, 1997 and Liu, 1996). In wet bulk micromachining, features are sculpted in the bulk of materials such as silicon, quartz, SiC and glass (e.g. diaphragms, suspension beams). It is done by orientation dependent (anisotropic) and/or orientation independent (isotropic) wet etchants. Figure 1-1 shows isotropic wet bulk etching process. The geometric shapes resulted from wet bulk etching process are not bounded by perfectly defined crystallographic planes. Hence this process is not used in the fabrication of commercial integrated circuits and sensors where anisotropy is the key for devices to work.
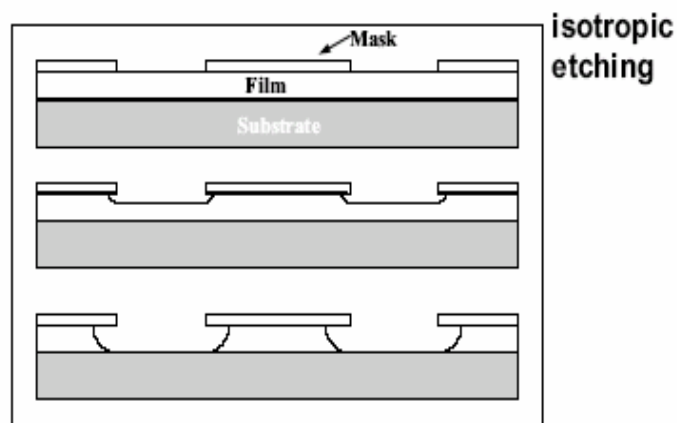
Figure 1-1 Isotropic wet bulk etching

For isotropic etchants (Figure 1-1), the etch rate is the same in all the crystallographic directions. The etchants are usually acidic such as Piranha (4:1, $H_2O_2:H_2SO_4$), Buffered HF (5:1, NH_4F:conc. HF) and HNA ($HF/HNO_3/CH_3COOH$). The etch rate is very temperature sensitive and agitation sensitive, making it difficult to control the geometries. Anisotropic etchants (Figure 1-2) results in geometric shapes bounded by perfectly defined crystallographic planes.
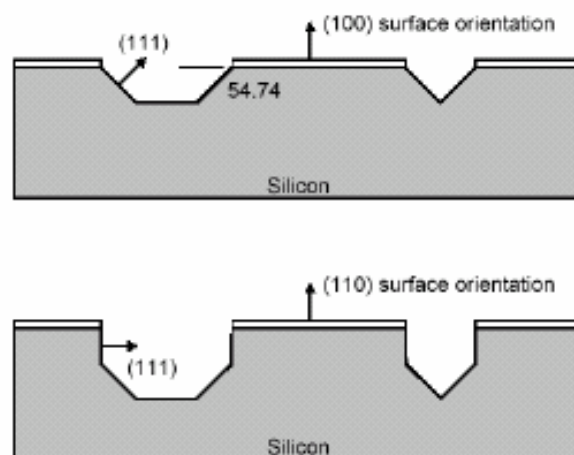
Figure 1-2 Anisotropic wet bulk etching

The most commonly used anisotropic etchants are Potassium hydroxide (KOH), Ethylene diamine pyrocatechol (EDP) and Tetramethyl ammonium hydroxide (TMAH). They are not agitation sensitive like isotropic etchants but suffer from slow etch rates (e.g. Etch rate ~ 1 µm/min in <100> direction for Si in KOH at 85 ^{0} C). The typical masking layers used in wet bulk micromachining are photoresist, thermal silicon dioxide, polysilicon, and LPCVD silicon nitride. This technique has been used in making several types of commercial sensors and for measuring pressure and acceleration.

In surface micromachining, (Figure 1-3), the features are built up, layer by layer, on the surface of a substrate.
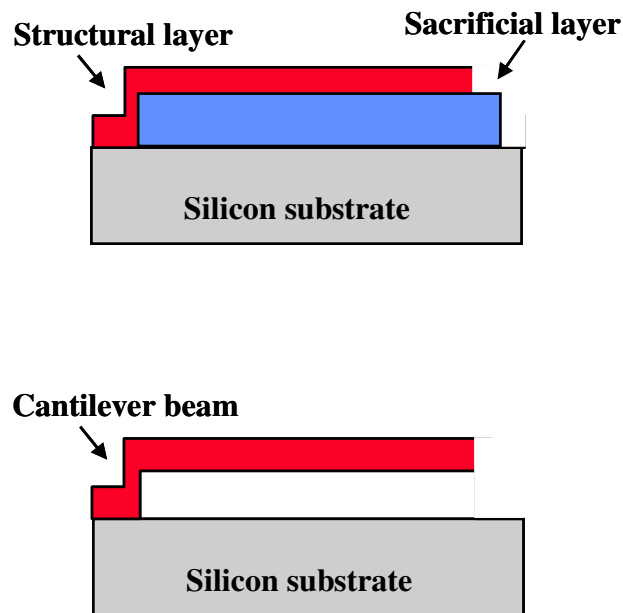
Figure 1-3 Surface micromachining technique

Here dry etching is used to define the surface features in the x,y plane and theses features are released from the plane by undercutting using wet etching. The structural layers are deposited over sacrificial layer. The sacrificial layer is removed by dry or wet

etch process form a free standing structures. The most commonly used sacrificial layers are, LPCVD phosphosilicate glass and a phosphorous doped (4-8 wt %) silicon dioxide. The common etchants for these layers is 49% hydrofluoric acid (HF). After removal of sacrificial layer, the wet process tends to cause sticking of suspended structures to the substrates due to the inherent proximity (less than a few microns). This problem is called stiction. Various drying techniques such as evaporation drying of DI water and sublimation drying with t-butyl alcohol can be used to avoid stiction.
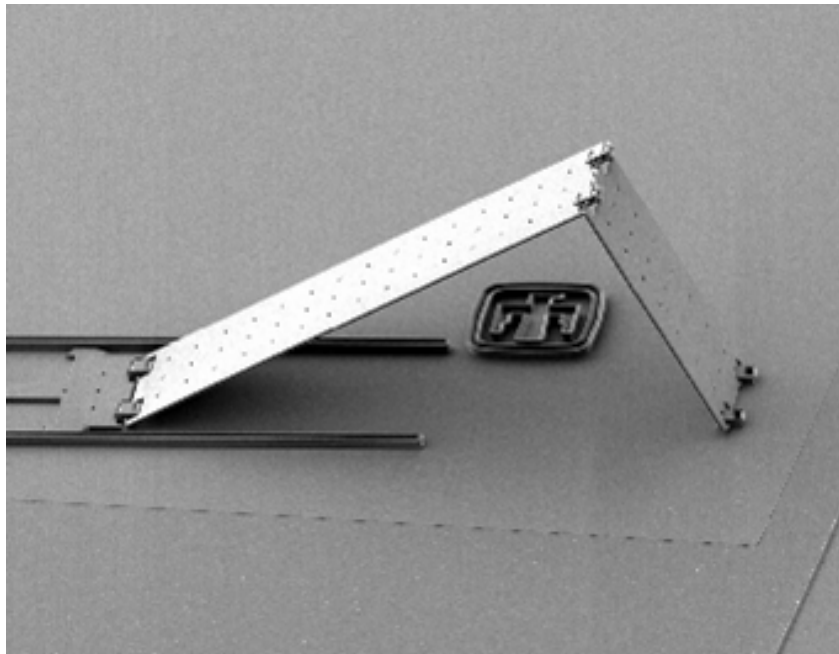
**Figure 1-4 Hinged mirror fabricated using silicon micromachining technology
(www.sandia.gov)**

A number of microstructures made from silicon nitride and polycrystalline silicon (e.g. gears, springs, microphones, hinged mirrors as shown in Figure 1-4) have been fabricated using surface micromachining.

Due to some of the limitations of wet bulk micromachining and surface micromachining techniques other processes such as silicon on insulator (SOI), hinged

7

poly-si, LIGA have been developed. LIGA is the German acronym for X-ray lithography (X-ray lithographie), electrodeposition (Galvanoformung), and molding (Abformtechnik). It involves a thick layer of X-ray resist, from microns to centimeters, and high energy X-ray radiation exposure and development to arrive at a three dimensional resist structure. LIGA process can be used to create structures with high aspect ratios. A wide variety of shapes from different materials with extreme low surface roughness can be achieved. This technique is limited due to expensive mask making and very high start up investment for synchrotron based X-ray lithography.

1.4 Microfluidics

Microfluidics is a subset of microsystem technology like MEMS. It is defined as a research discipline dealing with transport phenomena and fluid-based devices at microscopic length scales (Nguyen and Wereley, 2002). The small size scale causes changes in fluid behavior – some of which are beneficial. The projection considers four types of microfluidic devices: fluid control devices, gas and fluid measurement devices, medical testing devices, and miscellaneous devices such as implantable drug pumps. A fluid is a substance that deforms continuously under the application of shear. At conventional, macroscopic length scales, the fluid can be treated as a continuum. The density, velocity and pressure are defined at all points in space and vary continuously from point to point within a flow. This basic assumption of continuity of mass and other properties is not always true at microscopic length scales. If molecules of fluid are closely packed relative to the length scale of flow, this assumption is valid. On the other hand, if the molecules are sparsely distributed, then the assumption is invalid. E.g. a 10 µm channel contains 30,000 water molecules; hence it can be treated as a continuum.

The microfluidic devices such as microvalves, microchannels, various sensors, micropumps have been fabricated using an alternative technologies such as bulk micromachining, surface micromachining, deep reactive ion etching, LIGA etc. The modeling and simulation of these devices can be performed using computational fluid dynamic software like FLUENT, FEA software like ANSYS and MEMS software like COVENTOR. Please refer Figure 1-5 for the various fabrication processes to build the microchannels with different cross sections.
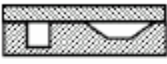
Channel Shapes	BM	SM	H	CM	WB
	✔		✔	✔	
	✔		✔	✔	✔
	✔			✔	
	✔				
	✔				
	✔	✔			
	✔		✔	✔	
		✔			

BM = bulk micromachining
SM = surface micromachining
H = high aspect ratio machining
CM = conventional machining
WB = wafer bonding

Figure 1-5 Summary of microchannel cross-sections and the fabrication technologies required to build them. (Grande, 2003)

The understanding of principles of microfluidics is essential to develop more complex systems that can handle increasingly demanding transport, manipulation, and timing requirements for a wide range of applications. An ideal microfluidic system enables complete analysis, from sample introduction (sample storage and injection), to pretreatment (concentrating, mixing, diluting and reacting), to the final analysis (separations, spectroscopy). Electroosmosis is one of the techniques that can be used for fluid transport. Electroosmosis is produced by the interaction of the solution layers near the solid/solution interface with an axial potential gradient. Thus, the space where fluid is processed has to be miniaturized to get a so-called lab-on-a-chip or micrototal analysis system and an array of applications can be achieved.

1.5 Motivation

Frame and Palmer (1999) have estimated shear stress from approximations of the velocity profiles determined by in-vivo particle tracking experiments in the hamster cheek. The accuracy of these estimations is limited by the assumptions that the tracking particles are neutrally buoyant and their trajectories follow a constant fluid streamline. Also, the 0.5 μm size of the microsphere flow markers yields a very coarse determination of velocity profile at the wall.

A computational fluid dynamics model has also been employed (Noren, 1999) to predict the shear stress in the vessel walls. Due to the non-Newtonian nature of the blood (due to the interactions of the red blood cells (RBC) with each other), these models are fairly complicated. Viscosity of the blood varies with RBC concentration (hematocrit levels). The uneven distribution of the RBC affects the local vessel geometry changing the viscosity. The size of RBC is ~5 μm relative to the vessel size ~17 μm. Hence it

requires the use of two phase flow dynamics, which are complicated by the deformability of the cells and the vessel walls. Due to these factors, it is difficult to model the exact nature of the flow at the time of vasoactive agent introduction.

Since there is no available method to directly measure wall shear stress in microcirculation, this thesis employs a silicon micromachining technology to integrate the micromachined thermal shear stress sensors with the microchannels $(17 * 17 \ \mu m^2)$ with bifurcation angles 30^0. The purpose is to measure wall shear stress at multiple locations in arteriole bifurcations (in vitro) while using water as a working fluid.

Chapter 2

Literature Review

2.1 Fluid Mechanics Concepts

2.1.1 Wall Shear Stress

The shear stress, τ, in the fluids is directly proportional to the velocity gradient (Hagen, 1999, Fox and McDonald, 1998). It can be written mathematically as Newton's law of viscosity,

$$\boldsymbol{\tau} = \boldsymbol{\mu}\frac{du}{dy} \tag{2-1}$$

where μ is the dynamic viscosity of fluid and $\frac{du}{dy}$ is the velocity gradient. Please refer Figure 2-1. The wall shear stress is the shear force per unit area exerted by a fluid tangential to the surface of a plate. Mathematically it can be expressed as,

$$\tau_w = \left(\mu \frac{du}{dy} \right)_{y=0} \tag{2-2}$$

where μ is dynamic viscosity of fluid and $\frac{du}{dy}$ is velocity gradient. The measurement of

wall shear stress is very difficult. The knowledge of wall shear stress is of primary

importance in aerodynamic and hydrodynamic design because it determines a major part

of aerodynamic drag. Please refer to Table 2-2 and 2-3 for a complete list of applications

of wall shear stress measurements.
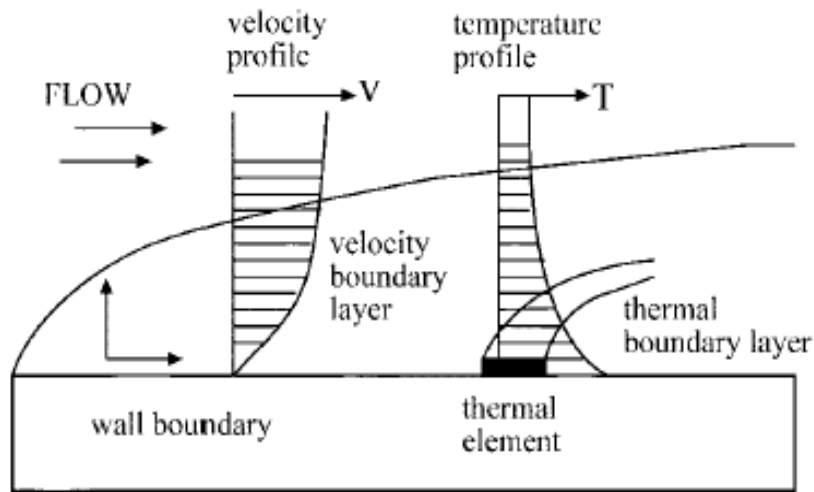
Figure 2-1 Velocity and thermal boundary layer (Liu, 1996)

The fluid in direct contact with the bottom surface has a zero velocity. The

velocity of the fluid changes linearly from zero at the bottom to free stream velocity, U_∞,

giving rise to a velocity gradient. This velocity gradient induces an exchange of

momentum from a region of high velocity to a region of low velocity, thus giving rise to

a momentum transfer. This momentum transfer is manifested as a shear stress in the fluid acting parallel to the direction of the fluid flow. The fluids that obey the Newton's law of viscosity are referred to as Newtonian fluids.

The boundary layer defined by fluid velocity, U, that satisfy the relation

$$\frac{U}{U_\infty} < 0.99 \qquad (2\text{-}3)$$

where U_∞ is the free stream velocity. Thus, velocity boundary layer is the region near the surface where the velocity increases from zero to 99% of the free stream velocity values. The flow has uniform velocity, U_∞ outside the boundary layer. In the boundary layer, the shear forces caused by viscosity are resisted by inertia forces in the fluid. The ratio of viscous force to inertial force is defined as the kinematic viscosity, υ,

$$\upsilon = \frac{\mu}{\rho} \qquad (2\text{-}4)$$

where μ is dynamic viscosity and ρ is density of fluid. For liquids, the dynamic viscosity decreases with increasing temperature.

2.1.2 Thermal Boundary Layer

Thermal boundary layer is a region near to a heated element in which a temperature gradient is present as shown in Figure 2-1. A fluid is flowing over a flat plate in Figure 2-1. The temperature of fluid at the leading edge of the flat plate is T_∞. Let the temperature of the plate be T_W. As the fluid flows and comes in contact with the heated plate, a thermal equilibrium is achieved. The heated fluid particles near the surface supply this thermal energy to the adjacent fluid layers. The thermal energy transfer reduces away from the surface and becomes negligible eventually when the temperature at that point

becomes equal to the free stream temperature, T_∞. The thermal boundary layer can be expressed mathematically for fluids at temperatures, T,

$$\frac{T_W - T}{T_W - T_\infty} < 0.99 \qquad\qquad (2\text{-}5)$$

where $T_W - T_\infty$ is the surface to free stream temperature difference.

2.1.3 Reynolds Number

Figure 2-2 shows a flow over a flat plate.
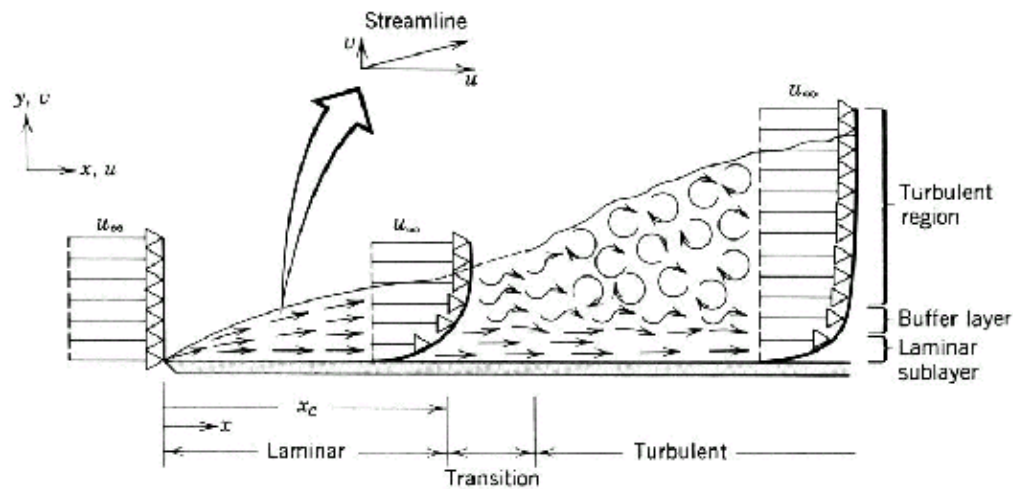
Figure 2-2 Laminar and turbulent boundary layers (Liu, 1996)

The viscous flow regimes can be divided into three regimes mainly: laminar, transitional and turbulent. In the laminar regime, flow structure is characterized by smooth motion in laminae, or layers. The moment interchange takes place between these laminas. There is no macroscopic mixing of adjacent fluid layers. If a thin filament of dye is injected into a laminar flow, it appears as a single line. The only dispersion in the flow is due to the slow diffusion by the molecular motion. Flow structure in the turbulent

15

regime is characterized by random, three dimensional motions of fluid particles in addition to the mean motion. The fluid particles show erratic motion with a large transverse of momentum. The macroscopic mixing of fluid particles from adjacent layers of fluid results in rapid dispersion of dye if introduced. The nature of flow (laminar or turbulent) is determined by the value of a dimensional parameter, the Reynolds number, Re.

For a fluid flow over a flat plate,

$$\text{Re}_x = \frac{\rho U x}{\mu} \tag{2-6}$$

where ρ is density of fluid, U is velocity of fluid, x is distance downstream from the leading edge of the plate, μ is viscosity of the fluid.

2.2 Shear Stress Measurement Techniques

The techniques to measure the wall shear stress (Haritonidis, 1989 and Hanratty, 1996) are limited as it is a parameter of small magnitude. The mean shear stress indicates the overall state of the flow over a given surface whereas the fluctuating stress provides information of the individual processes that transfer momentum to the wall. The various techniques for wall shear stress measurement can be classified into two broad methods: Direct and Indirect methods. Direct methods measure the wall shear stress directly while indirect methods infer the stress from the other measured properties. Figure 2-3 shows a schematic diagram of wall shear stress measurement techniques.
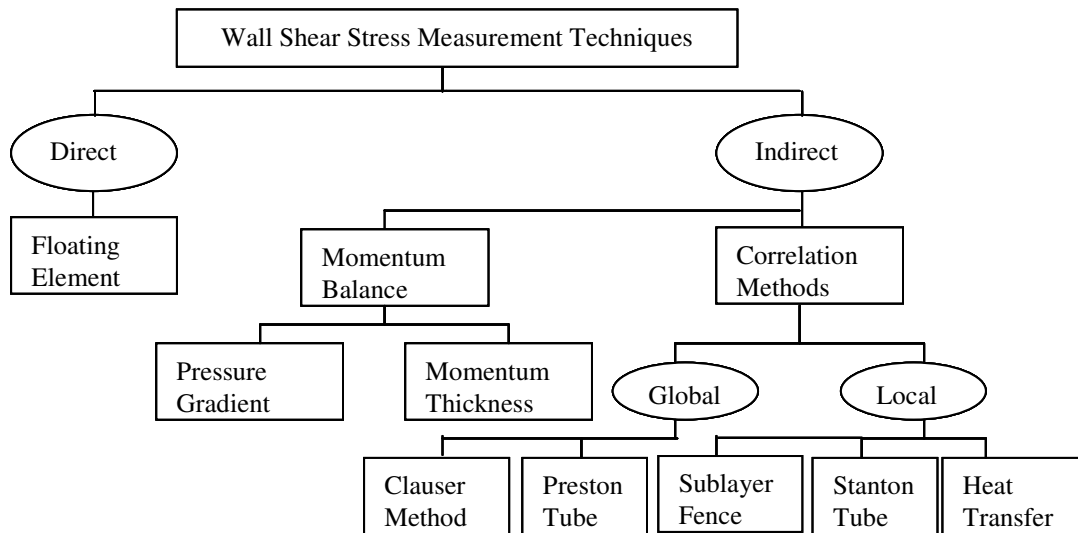
Figure 2-3 Wall shear stress measurement techniques (Haritonidis J. H, 1989)

2.2.1 Direct Measurement Techniques

Direct measurement techniques are ideal for measurement of wall shear stress because they sense directly the force applied by fluid to the wall. The techniques do not depend directly on the fluid properties.

The Floating element uses the compact gauges to measure directly the wall shear stress. The gauge is calibrated by using a static method. This technique requires a portion of the wall to be movable in a direction parallel to the boundary. The wall element is mounted on a balance. The balance is of two types either displacement balance, in which the displacement of the wall is correlated to the applied force or a feed back balance, where the force required maintaining the wall element at its original position is equal to the applied force.

The wall shear stress can be calculated once the force and the area of the element are known. Figure 2-4 shows a schematic of a floating element.
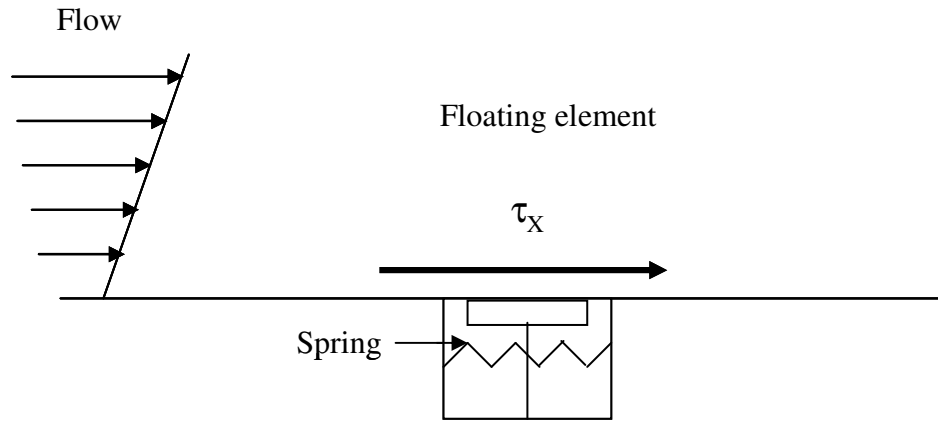
Figure 2-4 Floating element

The greatest advantage of this technique is that the wall shear stress is measured directly without any need to make any assumption about the fluid flowing above it. This technique suffers from some serious disadvantages that are listed in Table 2-1.

Table 2-1 Disadvantages of floating element

No	Disadvantages of floating element technique
1	The effect of the necessary gaps around the floating element
2	The effect of misalignment of the element with respect to the surrounding surface
3	Forces due to pressure gradient
4	The effects of heat transfer
5	The use in the presence of suction and blowing
6	The effects of gravity or acceleration if the device is to be used in a moving vehicle
7	The effects of temperature changes
8	The effects of leaks
9	The effects of the whole system in the presence of large transients

No	Disadvantages of floating element technique
10	Poor frequency response because of their large size. This makes the use of this method unsuitable in measuring the fluctuating shear
11	Due to very delicate nature of the device, it is difficult to handle and install
12	The compromise between the size of the transducer and the measurement of very small forces or deflections

2.2.2 Indirect Measurement Techniques

Momentum balance

There are two types of momentum balance techniques, pressure gradient and momentum thickness. The average wall shear stress for flows in constant area ducts, such as pipes or channels, can be obtained from the pressure gradient. The principal behind the operation is that the pressure drop over a given length of the duct is directly balanced by the integrated shear stress over the wetted surface of the same length. The important consideration in this method is that the pressure will be the same at any azimuthal position of the duct at a given duct position. This consideration will be true only if the duct possesses a radial symmetry and also the duct dimensions do not change along the duct length. For a duct with arbitrary cross sectional area A, the pressure drop over a given duct length L is given as,

$$\overline{\Delta P}A = \int_S \overline{\tau_x}ds \qquad (2\text{-}7)$$

where S is area over which the stress acts, A is cross sectional area of duct and τ_x is wall shear stress. For a circular pipe or channel,

$$\overline{\tau_x} A = \frac{1}{2} \frac{\overline{\Delta P}}{L} h \tag{2-8}$$

where h is pipe radius or height of channel. For accurate measurement of the pressure drop, the length L has to be long enough. The flow has to be fully developed in order to have all streamwise gradients of the flow quantities to be zero. It is an ideal method for calibration purposes.

Momentum thickness gradient uses Von Karman's momentum theorem to relate the mean wall shear stress to the momentum thickness while considering two-dimensional laminar or turbulent layers. The difficulty with this method is that wall shear stress depends upon the accurate measurement of the velocity profile. The other disadvantages are the tedious and time consuming nature of this method.

Correlation Methods

Correlation Methods can be classified as local and global techniques. Local methods depend on the flow field in the vicinity of the device used to measure the shear stress. Advantages of local method over the global one is that the flow field that affects the measurement is confined to a very small region of the flow near the wall and is not sensitive to the structure of the flow away from the wall.

The Clauser plot (Global) uses the logarithmic portion of the law of the wall to determine the wall shear stress. This method is useful for the majority of flows excluding low Reynolds number flows. It is necessary to accurately measure the velocity profile using hot-wires and laser-dopppler anemometers (LDA) to obtain the correct value of the wall shear stress. The Pitot tube can be used to measure the velocity profiles as it is much simpler to use. But errors like displacement of the effective tube height due to shear can be produced leading to an inaccurate reading.

Preston tube (Global) is the most common method used for the measurement of the average wall shear stress. The pressure measured by Preston tube is a Bernoulli-type pressure since it results from the deceleration of fluid in front of the tube. Hence it is a global device. The principal of operation of Preston tube is that they obey the equations for Pitot tube that has an effective center at a certain point proportional to the outside tube diameter. The Preston tubes are easier to fabricate and to operate and do not need to be calibrated. They suffer from some of the disadvantages with respect to the measurement of the wall shear stress. They give an obstruction to the flow. In the three dimensional boundary layers the direction of flow at the wall has to be known to orient the Preston tube properly.

The Stanton tube and Stanton gauge (Local) method was developed by Stanton in order to determine the fluid velocity close to a boundary, to find out the existence of slip at a wall for a turbulent flow. Stanton used a rectangular Pitot tube that had the wall of a pipe as one of its sides. The difference between the pressure measured with this Pitot tube and the static pressure was used to determine the velocity at the center of the tube. The experiments were carried out to establish a calibration curve for the "effective center point" of the Stanton tube. This was used to measure velocities in a fully developed turbulent flow. If the effective center of the Stanton tube was located close enough to the wall, the velocity calculated from the pressure measurement could be related to the wall shear stress.

The original design of Stanton has proved to be awkward to use and hence an alternative design in the form of the Stanton gauges have been suggested. The Stanton gauges are small in size. In this design a difference between two static pressures

calibrated against wall shear stress. In tests, comparing the performance of Stanton gauges and heated film gauges in the laminar boundary layers, it is found that the Stanton gauges give inaccurate reading in large unfavorable pressure gradients. The inaccurate readings result because they are being influenced by regions of the field where the velocity is not varying linearly with distance from the wall. The tests also indicated that Stanton gauges couldn't be regarded as reliable devices in the boundary layers with large pressure gradients.

In heat transfer or thermal methods (Local), the heat transfer from a suitable surface element to the fluid is related to the wall shear stress. The typical device that works on this principal is hot-film as shown in Figure 2-5.
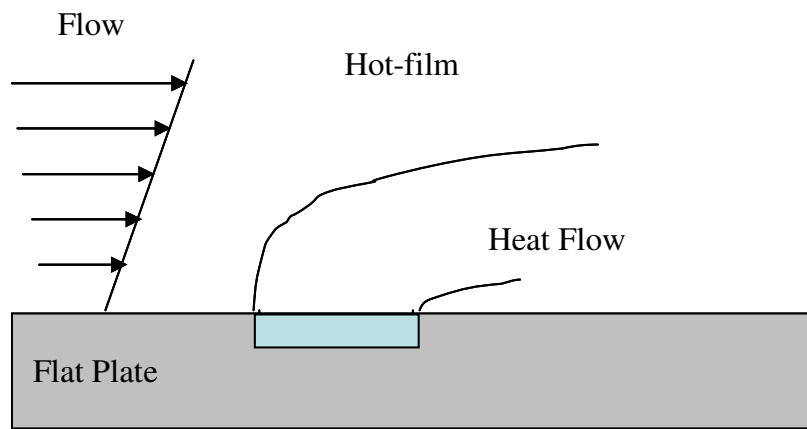
Figure 2-5 Heat transfer or thermal method

The hot-film is heated electrically. The joule heat generated, Q_J, in the hot-film is carried away by the fluid as well as conducted to the substrate. Q_f is the heat carried away by the fluid and Q_s is the heat lost to the substrate, Thus,

$$Q_J = Q_f + Q_s \qquad (2\text{-}9)$$

The basic assumption in order to relate wall shear stress with heat transfer is that the thermal boundary layer lies entirely within the linear region of the velocity boundary layer. The wall shear stress can be related to the heat transfer,

$$\tau_w \sim Q^3{}_f \qquad (2\text{-}10)$$

where τ_w is wall shear stress and Q_f is given by

$$Q_f = Q_{f1} + Q_{f2} \qquad (2\text{-}11)$$

where Q_{f1} is heat transfer rate to the fluid directly from the heated surface and Q_{f2} is heat transfer rate to the fluid indirectly through the heated portion of the substrate.

Equation (2-10) is only valid for steady, laminar and zero pressure gradient flow. In the case of unsteady and turbulent flow most of the assumptions made for deriving equation (2-10) fail and hence we can not use this equation. The thermal method will be discussed in more detail in Section 2.3.2.

Sublayer fence consists of a wall obstruction completely immersed in the viscous sublayer. The height of the fence can be varied with a screw mechanism. The difference in pressure before and behind a sharp edge projecting through the surface, normal to the flow, is related to the wall shear stress. The advantages of this instrument over the Stanton gauge are that it gives an almost doubled pressure reading. Also the height of the fence can be smaller than that of Stanton gauge because of the larger pressure readings. It eliminates the necessity of a separate static pressure tapping and also gives readings in both forward and reversed flows. The tests show that the Sublayer fence is of unknown accuracy in flows with strong pressure gradients.

2.3 Micro-machined Shear Stress Sensors

The conventional methods as discussed in the above section allow only a certain degree of miniaturization because their manufacturing requires delicate handicraft. The conventional devices are more or less hand made, thus making mass-production with good device repeatability very difficult to achieve. Today, smaller sensors are needed in order to improve the accuracy, flexibility and resolution of these methods. The length scale matching between the sensors used and the investigated phenomena is essential. Due to the advent of MEMS, the conventional sensor sizes can be miniaturized. MEMS promises to fabricate these sensors with extremely small tolerances with a reasonable cost. These miniature sensors can be integrated with microelectronics to achieve sensing, information processing and actuation on a single chip. The integration can greatly reduce the total number of external electrical leads. This is especially advantageous for a distributed control system where a large number of sensor arrays are present. On chip electronics reduces the electromagnetic interference from outside and parasitic effects from the external leads. Both indirect and direct shear stress measurement techniques have been implemented using bulk and surface micromachining technology. Out of all conventional methods discussed in the above section, floating element and thermal methods are best suited for MEMS fabrication. Table 2-2 and 2-3 lists some of the recently developed MEMS-based micro-machined shear stress sensors. The interdisciplinary research of using MEMS devices in fluid mechanics and aerodynamics is creating opportunities and challenges and hence new results in these fields are being discovered.

Table 2-2 Floating Element Type Shear Stress Sensors

Shear Stress Sensors-Floating Element type - Direct measurement									
Sr. No.	Investigators	Research School	Type	Dimensions	Range	Sensitivity	Application	Fabrication Technology	Reference Citation
1	Schmidt et al. (1988)	MIT	Floating element type	$500*500 \ \mu m^2$	1-12 Pa	7.5 nm/Pa	To determine mean value and fluctuating shear stress	Surface Micromachining of polymide	IEEE (1988) Ph. D. Thesis (1988)
2	Padmanabhan et al. (1997)	MIT	Floating element type	$500*500*7 \ \mu m^3$	0.0014-10 Pa		To characterize turbulent boundary layer		Ph. D. Thesis (1997)
3	Roche et al. (1996)	France	Floating element type sensor using Piezoelectric bimorph bending (direct)	$29*24* 13 \ mm^3$ (global)	1-100 mN rms	220 nC/N	Measure the mean shear stress to get a better understanding of boundary layer and flow noise coupling		Sensors and Actuators (1996)
4	Roche et al. (1996)	France	Floating element type sensor using Piezoelectric bimorph bending (direct)	$22*20*14 \ mm^3$ (global)		212 nm/V (8 bimorph)	measure the mean shear stress to get a better understanding of boundary layer and flow noise coupling		IEEE(1996)
5	Pan (1996)	Case Western Reserve University, Ohio	Floating element type	$100*100 \ \mu m^2$	0-25 Pa		Fabrication of floating element type micromachined sensor	Surface Micromachining and IC processing	Ph.D Thesis (1996)
6	Hyman (1996)	Case Western Reserve University, Ohio	Floating element type	$100*100 \ \mu m^2$	0-25 Pa	9.2 and 5.7 Pa/micron	Fabrication of floating element type micromachined sensor: testing and calibration	Surface Micromachining and IC processing	M.S. Thesis (1996) Hyman et.al ICIASF 1995

Sr. No.	Investigators	Research School	Type	Dimensions	Range	Sensitivity	Application	Fabrication Technology	Reference Citation
7	Lofdahl et al. (1999)	Chalmers University of Technology, Sweden	Thermal, Floating element type sensors		0.003-10 Pa		to measure fluctuating wall shear stress in turbulent flows		Meas. Sci. Technology (1999)
8	Pan et al. (1999)	Case Western Reserve University, Ohio (2 papers)	Floating element type sensor (direct)	100 µm beam 120 µm beam	0.5 - 3.5 Pa	1) 9 and 5.5 pa/ micron of floating element deflection 2) 1.02 V/ Pa +/- 5%	to measure wall shear stress to determine aerodynamic drag, aircraft stall	Polysilicon surface micromachining technology	AIAA Journal (1999)
9	Jiang et al. (2000)	Caltech	Flexible micromachined based Shear stress sensor array	1* 3 cm^2 (> 100 sensors)		100 mV/Pa	flow separation point detection over a circular cylinder and leading edge of a delta wing	Surface/Bulk Micromachining	Sensors and Actuators (2000)

Table 2-3 Thermal Type Shear Stress Sensors

Sr. No.	Investigator	Research School	Type	Dimensions	Range	Sensitivity	Application	Fabrication Technology	Reference Citation
Shear Stress Sensors-Thermal type - Indirect measurement									
1	Liu et al. (1994)	Caltech, UCLA, UIUC	Hot film sensor	$200*200*15$ μm^3			To calculate viscous drag experienced by an object	Surface micro-Machining	IEEE (1999)
2	Liu et al. (1994)	Caltech, UCLA	Thermal Shear Stress Sensor	$2 * 2$ cm^2 sensor package	0.1 - 1.4 Pa	15 V / Kpa	Surface drag reduction in turbulent flow	Surface Micro-machining	ASME (1994)
3	Liu (1996)	Caltech	Thermal sensor	$200*200$ μm^2 – cavity diaphragm	0.2-0.7 Pa		To identify flow separation lines along the delta wing's leading edge	Surface Micro-machining	Ph.D Thesis (1996)
4	Jiang et al. (1996)	Caltech	Hot wire sensor (Indirect)	$2.85* 1$ cm^2 (50 sensors)	0.2-1 pa		Image surface shear stress distribution	Surface Micro-machining	IEEE(1996)
5	Gupta (1996)	Caltech	Thermal type shear stress sensor	25 sensors -[7.5 mm length]			To reduce the high shear stress on the surface and lower the total drag	Surface Micro-machining	IEEE (1996)
6	Gupta (1997)	Caltech	Hot-wire sensor	$150*3*0.4$ μm^3 wire	0.45-4.5 Pa		To diminish the impact of drag-inducing structures in the fluid		Ph.D (1997)
7	Jiang (1998)	Caltech	Hot wire sensor-	array of 100 sensors on a $1*2.85$ cm^2 chip	0.2 -1 Pa		To measure shear stress	Combined surface and bulk micro-machining	Ph.D.Thesis (1998)
8	Xu et al. (2000)	Caltech	Hot film sensor-Shear stress sensor based mass flowmeter				Directly measures mass flow rate using shear stress sensor	Surface micro-machining	IEEE(2000)

Sr. No.	Investigator	Research School	Type	Dimensions	Range	Sensitivity	Application	Fabrication Technology	Reference Citation
9	Jiang et al. (2000)	Caltech	Hot film sensors	36 sensors spanning the distance of 19.6 mm	0.1-0.9 Pa		Shear stress sensors used for the aerodynamic study of low-altitude unmanned aerial vehicles	Surface micro-machining	IEEE (2000)
10	Jiang et al. (2002)	Caltech	Thermal Shear Stress Sensor	210*210*4 μm^3	0.2-5 Pa	0.31 -1.10 V / Pa	To measure wall shear stress for underwater applications such as the flow field measurement of radio-controlled submarines and the safety and arming device of torpedoes	Surface micro-machining	IEEE (2002)
11	Huang (1995)	UCLA	Hot film sensor w/ and w/o cavity underneath	200*200*2 μm^3 cavity			To determine wall shear stress	Surface Micro-machining compatible with IC technology	IEEE (1995)
12	Huanget al. (1999)	UCLA	Micro-Thermal Sensor	80*2 μm^2 for type I sensor	0.67-1		To measure the surface shear stress		Meas. Sci. Technology (1999)
13	Admiraal (1999)	Univ. of Illinois at U-C	Hot film sensor (Indirect)		0.03-10 Pa		To measure wall shear stress		Ph.D. Thesis (1999)

Sr. No.	Investigator	Research School	Type	Dimensions	Range	Sensitivity	Application	Fabrication Technology	Reference Citation
14	Outdhusden et al (1988)	Delft University of Technology, Netherlands	Thermal flow sensor(Indirect)	4* 3 mm^2 (sensor chip size)	0.1-1.6 Pa		Measure skin friction (wall shear stress) to observe aircraft stall behavior, airfoil maximum lift and maximum diffuser angles	Standard bipolar IC fabrication process	Sensors and Actuators (1988)
15	Drolet (1992)	University of Toronto	Heated film sensors	0.1* 1 mm^2 - active area of sensor			To measure skin friction		MS Thesis (1992)
16	Gottmann (1997)	The University of Arizona	Hot-film Sensor and Floating Element sensor	Hot film: 10*12*0.5 mm^3 chip with 12 different hot film elements (supplied) Sensor: 5 * 90 µm^2 {They could not implement the floating element}	1-50 Pa		An experiment to study vertical annular air-water flows in a channel with a rectangular cross section		Ph.D Thesis (1997)
17	Nagaoka et al. (1997)		Hot film sensor (Indirect)	200* 200 µm^2		100 mV/Pa	To obtain information on the separation characteristics associated with the phenomenon of stall		JSME International Journal (1997)
18	Kimura et al. (1999)	Nihon Univ, Japan	Thermal type shear stress sensor	25 sensors -[7.5 mm length]		1 V / Pa	To determine correlation between peak shear stress level and front end shear slope of a high shear stress streak		Fluid Dynamics research (1999)

29

2.3.1 Floating Element Type Sensors

The floating element technique (Padmanadhan, 1997) is a direct method for sensing the wall shear stress. A direct measurement of the tangential force exerted by the fluid on a specific portion of the wall can be done.
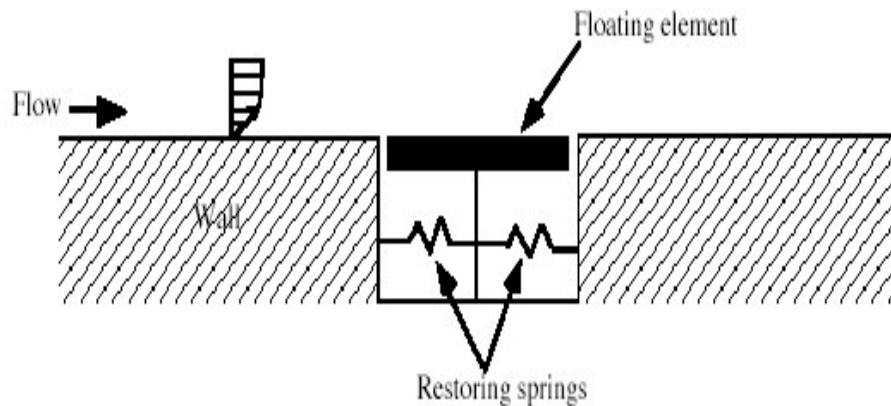
Figure 2-6 Floating element type sensor

The principle behind operation of floating element is that a fluid exerts a shear force on the surface of the floating element which is balanced by the restoring force of the spring. Thus, the restoring spring force balances the shear force exerted by the fluid. This relationship can be expressed as

$$K\delta = \tau_w A \tag{2-12}$$

where K is spring constant, δ is displacement of the floating element, τ_w is wall shear stress and A is surface area of the floating element.

The major advantage of this method is that the wall shear stress is determined without making any assumptions about the flow field above the device. The sensing wall element is connected to a balance that determines the magnitude of the applied force.

In summary, the advantages of the floating element method are that it is a direct technique for local wall shear stress measurement and it can be used to calibrate various indirect measurement techniques. Some of the drawbacks of floating element method are as follows: This technique requires a portion of the wall to be movable in a direction parallel to the boundary. Due to this requirement, the sensing element must have a gap around its perimeter. As a result, wall shear stress in the regions close to the gap is altered. Fluid circulation can occur through the gap in the presence of pressure gradients; however, this is only significant in large pressure gradient flows. If gap size is less than a few viscous length-scales, it will not disturb the flow. Another disadvantage is that the sensor size must be at least four times the viscous length for accurate measurement of wall shear stress. (E.g. : Viscous length is determined to be 30 µm for the measurement of shear stress in the turbulent boundary layer flow at MIT according to Padmanadhan 1997. Hence the sensor size required was 120 µm * 7 µm). Also, due to pressure gradients in the flow results in an inaccurate value of shear stress. The percentage of this error can be as high as 50 % in case of large pressure gradient flows.

2.3.2 Thermal Shear Stress Sensors

The thermal sensors are of two types: hot film and hot wire, as shown in Figure 2-7. Hot wire sensor consists of a micromachined hot wire close to a wall. Hot wire, usually a polysilicon resistor, is supported by two long arms that are placed on a solid substrate. The wire is in a linear velocity distribution region and thus measures wall shear stress instead of velocity.
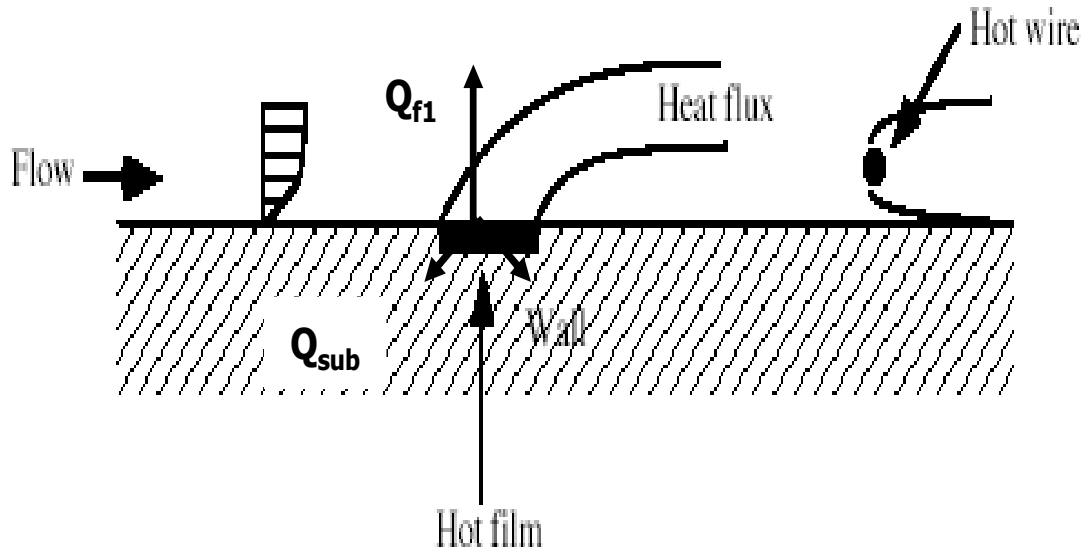
Figure 2-7 Hot film and hot wire type thermal sensors

Hot film sensors consist of a sensing element made of polysilicon resistors. The resistor rests on the silicon nitride diaphragm to provide thermal isolation. Metal leads connect the sensor to electronic circuitry through bonding pads. The principle behind operation of hot film sensor is that the heat transfer from a sufficiently small heated surface depends only on the flow characteristics in the viscous region of the boundary layer. The hot-film consists of a thin metallic film flush mounted into a substrate. The gauge forms one part of a wheatstone bridge. An electric current is passed through a film in order to maintain it at a constant temperature as heat is continuously being transferred from the film to the moving fluid as well as to the film's substrate. The change in the temperature of sensor is measured by the change in the film resistance. If the flow is steady and laminar then resulting heat transfer rate to the fluid can be related to the wall shear stress by an empirical relation as discussed in Section 2.2.2.
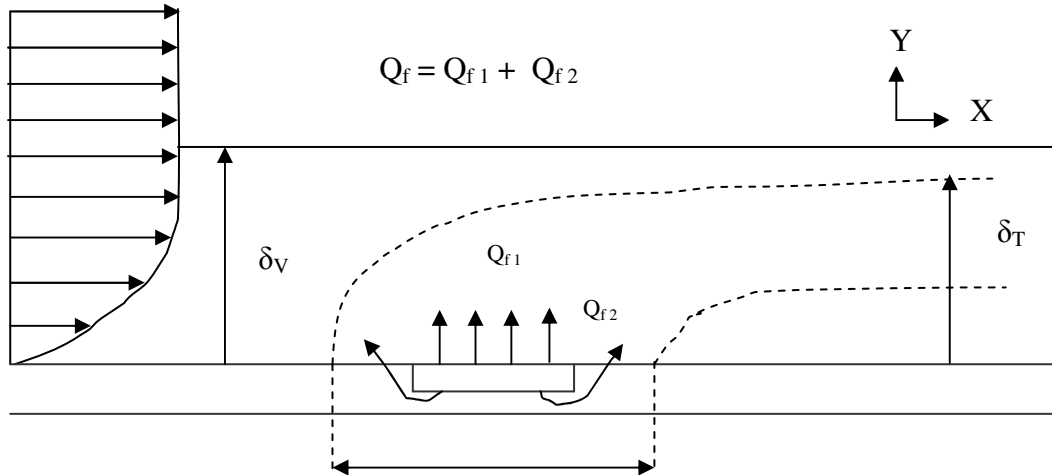
Figure 2-8 Two dimensional thermal hot film sensor

Consider a two-dimensional wall element as shown in Figure 2-8 aligned with its long side (going in to the plane of paper) perpendicular to the direction mean flow (Hanratty et al., 1996, Liu, 1996, Lofdahl et al., 1999). The fluid at the surface of the wall element is controlled at a temperature T_W, which is different from that in the bulk fluid (T_B). The rate of heat transfer between the fluid and the wall element is then measured. If the element is small enough in the flow direction then the thermal boundary layer over the element will be thin. It can be assumed that the thermal boundary layer lies within the velocity boundary layer. A velocity in this region is given by

$$U_y = Sy \qquad (2\text{-}13)$$

where $S = \dfrac{d}{dy} U_y$ is the magnitude of the velocity gradient at the wall, U is stream wise velocity of fluid at a distance y, normal to the wall.

A calibration is established between the measured heat transfer rate and the velocity gradient S. The wall shear stress can be evaluated by the following equation once the viscosity of the fluid is known,

$$\tau_w = \mu S = \mu \frac{d}{dy} U_y \qquad (2\text{-}14)$$

where τ_w is wall shear stress and μ is fluid viscosity.

The analytical expression for the calibration can be derived under the following 6 major assumptions and conditions:

1. The scalar boundary layer is within the region where U = Sy.

2. The flow is homogeneous over the surface of the element.

3. δ_T (thickness of the thermal boundary layer) is small enough compared to the width W of the hot film so that diffusion in the spanwise direction can be neglected.

4. Forced convection is large enough so that diffusion in the x-direction can be neglected.

5. Natural Convection is small compared to the forced convection.

6. The scalar boundary layer is small enough so that the influence of turbulent transport in the y direction can be neglected.

The heat balance equation for a two-dimensional field is given as

$$\rho C_p \left(\frac{\partial T}{\partial t} + (Sy)\frac{\partial T}{\partial x} + V \frac{\partial T}{\partial y} \right) = \alpha_T \left(\frac{\partial^2 T}{\partial x^2} + \frac{\partial^2 T}{\partial y^2} + \frac{\partial^2 T}{\partial z^2} \right) \qquad (2\text{-}15)$$

where ρ is fluid density, C_p is heat capacity of fluid, T is temperatures, V is normal component of fluid velocity, α_T is thermal diffusivity { $\alpha_T = \frac{K_T}{\rho C_p}$ } and K_T is thermal conductivity of the fluid. Because of assumption 1, Sy is substituted for U.

Assumptions 2, 5 and 6 allow for $V\dfrac{\partial T}{\partial y}$ to be neglected. Assumptions 3 and 4 allow for

$\alpha_T\dfrac{\partial^2 T}{\partial z^2}$, $\alpha_T\dfrac{\partial^2 T}{\partial x^2}$ to be neglected.

Equation (2-15) can be simplified to

$$\rho C_p\left(\frac{\partial T}{\partial t}+(Sy)\frac{\partial T}{\partial x}\right)=\alpha_T\left(\frac{\partial^2 T}{\partial y^2}\right) \tag{2-16}$$

If a pseudo-steady state assumption is made, then

$$\rho C_p\left((Sy)\frac{\partial T}{\partial x}\right)=\alpha_T\left(\frac{\partial^2 T}{\partial y^2}\right) \tag{2-17}$$

Equation (2-17) can be solved by applying the following boundary conditions,

$$T = T_w \quad \text{for } y = 0 \tag{2-18}$$

$$T = T_B \quad \text{for large } y \text{ and } x = 0 \tag{2-19}$$

From the solution given by Mitchell and Hanratty (Hanratty and Mitchell, 1966), the average heat transfer rate can be calculated, since

$$q = \frac{1}{L}\int_0^L \alpha_T\left(\frac{\partial(\rho C_P T)}{\partial y}\right)_{y=0}\ \mathrm{dx} \tag{2-20}$$

where q is rate of heat transfer per unit area and L is length of hot film sensor. A heat-transfer coefficient h can be defined as (Hanratty and Mitchell, 1966)

$$h = \frac{\langle q\rangle}{(T_B - T_W)} \tag{2-21}$$

where $\langle q\rangle$ is spatial average of the local rate of heat transfer per unit area, T_B is the bulk temperature of the fluid and T_W is the temperature of the fluid at the wall. A heat-transfer coefficient h can further be expressed as (Hanratty and Mitchell, 1966)

$$h = 0.807 \frac{C_P^{1/3} K_T^{2/3} \rho^{1/3} \tau_w^{1/3}}{L^{1/3} \mu^{1/3}} \qquad (2\text{-}22)$$

Thus the theoretical design equation for hot film sensor can be written as

$$\frac{q}{\Delta T} = 0.807 \frac{Cp^{1/3}}{L^{1/3}} \frac{K_T^{2/3}}{\mu^{1/3}} (\rho \tau_w)^{1/3} \qquad (2\text{-}23)$$

Since the heat loss from the hot film sensor is related to the heating current I and the resistance by the relation

$$q = I^2 R / A_e \qquad (2\text{-}24)$$

where A_e is area of the hot film sensor and R is the hot film resistance. Equation (2-23) can be written in the form

$$\frac{I^2 R}{\Delta T} = A (\rho \tau_w)^{1/3} \qquad (2\text{-}25)$$

where A is the parameter used to characterize hot film sensor and is given by

$$A = 0.807 A_e C_p^{1/3} K_T^{2/3} / L^{1/3} \mu^{1/3}$$

A is a weak function of temperature. Since part of the input power is supplied to the fluid and rest is lost through substrate, the power balance can be expressed as

$$\frac{I^2 R}{\Delta T} = A (\rho \tau_w)^{1/3} + B \qquad (2\text{-}26)$$

The term B (the heat loss to the substrate) should be smaller than $A(\rho \tau_w)^{1/3}$ (the heat loss to the fluid) to obtain the higher sensitivity. The effective length of the thermal element calculated from experimentally determined values of A is found to be many times larger than the actual length of the heating element. This is because the heat gets transferred to the fluid from both the heating element and the substrate. The large heat loss to the substrate is one of the major concerns in the use of hot film sensors. At smaller

τ_w values the sensitivity of the instrument to changes in τ_w diminishes. Since the heat loss to the substrate and the effective length of the hot film are difficult to predict, the hot film sensors must be calibrated to determine A and B. Thus, while in order to design a successful hot film shear stress sensor, the heat loss to the substrate must be minimized.

The major advantages of thermal shear stress sensors (Liu, 1996; Padmanabhan, 1997) are that they can achieve high sensitivity in low shear environment, with a small sensor size. They can be used in a wide variety of flow conditions. The sensor is flush mounted on the surface hence it provides minimal disturbance to the flow itself. They offer the possibility of measuring time varying flow and can operate in high pressure gradients.

The major disadvantages of thermal shear stress sensors (Padmanabhan, 1997) are that they suffer from calibration and repeatability problems due to substrate conductivity. In particular, measurements in high-frequency fluctuating flows have presented uncertainties. Also, this wall shear stress measurement technique depends on correlations (heat to momentum transfer analogies) to relate measured flow properties to the wall shear stress. Hence the accuracy of the shear stress depends upon the accuracy and validity of these empirical and semi-empirical correlations.

2.4 Microchannels and Blood Flow

The information about blood flow can be obtained by two approaches (Walburn et al. 1976), an experimental approach in which an *in vitro* model of the *in vivo* blood flow circulation system is constructed and relevant information can be obtained from the model. Another experimental approach is to obtain the information directly from an

animal. In mathematical modeling approach, a mathematical model of the *in vivo* blood flow situation can be developed. An empirical constitutive equation for a whole human blood can be obtained to describe the behavior of blood.

A blood is a non-Newtonian fluid. The viscosity of whole blood decreases as the rate of shear increases (Pseudo plastic behavior). The whole blood exhibits a yield stress i.e. a certain minimum force is required to initiate a flow (Bingham plastic behavior). Thus a constitutive equation chosen for blood is the power law equation as follows,

$$\tau = k(\dot{\gamma})^n \tag{2-27}$$

where τ is shear stress (dyn / cm^2), $\dot{\gamma}$ is shear rate (sec^{-1}), k is consistency index ($P\text{-}sec^{n-1}$) and n is the Non-Newtonian index.

The validity of this expression has been examined for shear rates in excess of 23.28 S^{-1}. The values of k and n are assumed to be constant for a given composition and a given hematocrit level. Table 2-4 for some of the review papers on blood flow in microchannels. Thus, after thorough literature search the following gap in the research is observed: No study has been done in microchannels that include blood as the working fluid, bifurcations in the microchannels or shear stress measurements using thermal sensors. Hence this thesis work is an effort to investigate the wall shear stress by means of thermal hot film sensors in the microchannels with bifurcation angles 30^0 using water as a working fluid

Table 2-4 Review papers on blood flow in microchannels

Author	Microchannel size	Comments
Chang et al. (2001)	$200*60\ \mu m^2$	Measured pressure drop vs. volumetric flow rate for blood. Theoretically determined apparent viscosity vs. shear rate
Tracey et al. (2000)	$3.5*3.2*100\ \mu m^3$	Developed a complete instrument for the measurement of erythrocyte (Red Blood Cell i.e. RBC's) flow in microchannels
Minamitani et al. (2000)	$9.1*10*130\ \mu m^3$	Studied mechanical properties (spring constant and Young's modulus) of RBC's. Atomic force microscope for the analysis of RBC elasticity and transparent microchannel flow system for analysis of RBC deformability
Frame et al. (1995)	20-50 μm in diameter	Microchannels fabricated in borosilicate microscope slide glass. An *in vitro* endothelial cell (A thin layer of cells that lines serous cavities and blood vessels) culture system can be used to examine responses to flow, which mimic the arteriolar microcirculation
Kikuchi et al. (1994)	$6*20\ \mu m^2$	Studied RBC deformability and transit times for 33 healthy male subjects aged between 24 and 63. Decrease in RBC deformability due to diabetes, is responsible for hypoxic (Deficiency in the amount of oxygen reaching body tissues) disturbances in tissues.
Kikuchi et al. (1992)	Equi. dia. = 6 μm, length = 14.4 μm	This structure was used to microscopically observe flow behavior of blood cells through the entire channel. The total volume flow rate of blood under constant suction was measured

Chapter 3

Modeling in Fluent

3.1 Fluent/Gambit Software

Computational fluid dynamics (CFD) is a computational technology that enables to study the dynamics of things that flow. Using CFD, one can build a computational model that represents a system or device that one wants to study and then apply the fluid flow physics to this virtual prototype. The software then outputs a prediction of the fluid dynamics. CFD is a sophisticated analysis technique. It not only predicts fluid flow behavior, but also the transfer of heat, mass (such as in perspiration or dissolution), phase change (such as in freezing or boiling), chemical reaction (such as combustion), mechanical movement (such as an impeller turning), and stress or deformation of related solid structures (such as a mast bending in the wind). Analysis of the fluid flow and heat

transfer inside microelectromechanical (MEMS) / microfluidic systems require specialized models as viscous forces dominate the inertial forces at micro-level. Fluent software provides advanced features such as fluid/structure interaction, free surface tracking with the volume of fluid method (VOF), and electrohydrodynamics. Typical applications include microfluidics, ink jets and ink jet actuators (including piezoelectric effects), and electrophorectic transport of tiny fluid samples. (www.fluent.com)

The three features involved in modeling and analysis software are preprocessing, processing and postprocessing. Preprocessing is the first step in which the model is built or imported from a CAD (GAMBIT , G/Turbo, TGrid or any other compatible with Fluent) package. This model is then meshed using a suitable meshing scheme and size. During processing, the CFD solver performs the calculations and produces the results. The material, fluid properties and the boundary conditions need to be applied before processing. Post processing is the final step in the CFD analysis, in which the data and images are organized and interpreted by means of contours, path lines, graphs etc.

Gambit is the meshing tool that is used to generate the mesh model to be fed into Fluent. Gambit has all the basic functions which could be found in any CAD package. However the modern tools such as blending and curving are not found in Gambit. A primary reason for this is attributed to the fact that the CFD code requires a well defined vertex/node for solving all the three basic fluid equations at each of the nodes. The basic steps in Gambit can be classified into the primary three : Model Creation, Mesh Generation, Exporting Files. The following represents the general sequence of operations in Gambit: Initial set up consists of primarily selecting the solver and the default values. Geometry creation consists of either importing the geometry or creating the geometry and

decomposing it into meshable sections. Meshing step consists of meshing the geometry depending on the criterion it meets. Zone assignments consist of applying the boundary conditions. Finally, export the mesh into the working directory.

Fluent provides two different solver formulations segregated and coupled. The segregated solver solves the continuity, momentum, energy and species equations sequentially. It has been traditionally used for incompressible and mildly compressible flows. This is the default solver in Fluent. The coupled solver solves the continuity, momentum, energy and species equations simultaneously. This is designed for high speed compressible flows. The coupled solver can be either a implicit or explicit. The implicit is used for highly coupled flows with strong body forces (e.g. buoyancy or rotational forces), or flows being solved on very fine meshes. It requires more memory but leads to faster convergence than the segregated solver. The explicit is generally used when less memory is present in the machine. It takes a longer to time to converge compared to the implicit solver.

To summarise , the procedure involved in the CFD analysis using Fluent software can be broken down to the following steps: Create the model geometry and grid. Start the appropriate solver for 2D or 3D modeling. Import the grid. Check the grid. Select the solver formulation. Choose the basic equations to be solved: laminar or turbulent (or inviscid), chemical species or reaction, heat transfer models, etc. Identify additional models needed: fans, heat exchangers, porous media, etc. Specify material properties. Specify the boundary conditions. Adjust the solution control parameters. Initialize the flow field. Calculate a solution. Examine the results. Save the results if necessary, refine the grid or consider revisions to the numerical or physical model.

3.2 Microchannel Model Description

There is a need to create and analyze a three dimensional MEMS model of thermal sensors integrated with microchannels ($17*17$ μm^2) in the Fluent software. The MEMS model consisted of microchannel on top, flush mounted polysilicon resistor in silicon nitride as the top layer of the sensor, the silicon dioxide in the middle as the insulating layer and the adequate section of silicon wafer as a substrate at the bottom to avoid errors due to end effects. The MEMS model had been used to simulate the system's thermal response to the constant temperature control circuit. The polysilicon resistor was held constant at 310 K and using a control system approach, power requirements for the hot film sensor were calculated. The model had also been used to optimize the sensor dimensions. The minimization of substrate heat loss is of prime importance in the design of thermal hot film sensors. A SiO_2 thickness underneath the polysilicon resistor (hot film) was varied and an optimum value of SiO_2 thickness was obtained to minimize the substrate heat loss. Also polysilicon thickness was varied and its value was optimized for minimum substrate heat loss.

The designer of a MEMS device requires a high level of fabrication knowledge in order to create a successful design. Often the development of even the rudimentary MEMS device requires a dedicated research effort to find a suitable process sequence for fabricating it. Hence a process sequence was first decided and then a MEMS model was created in Fluent as shown in Figure 3-1.
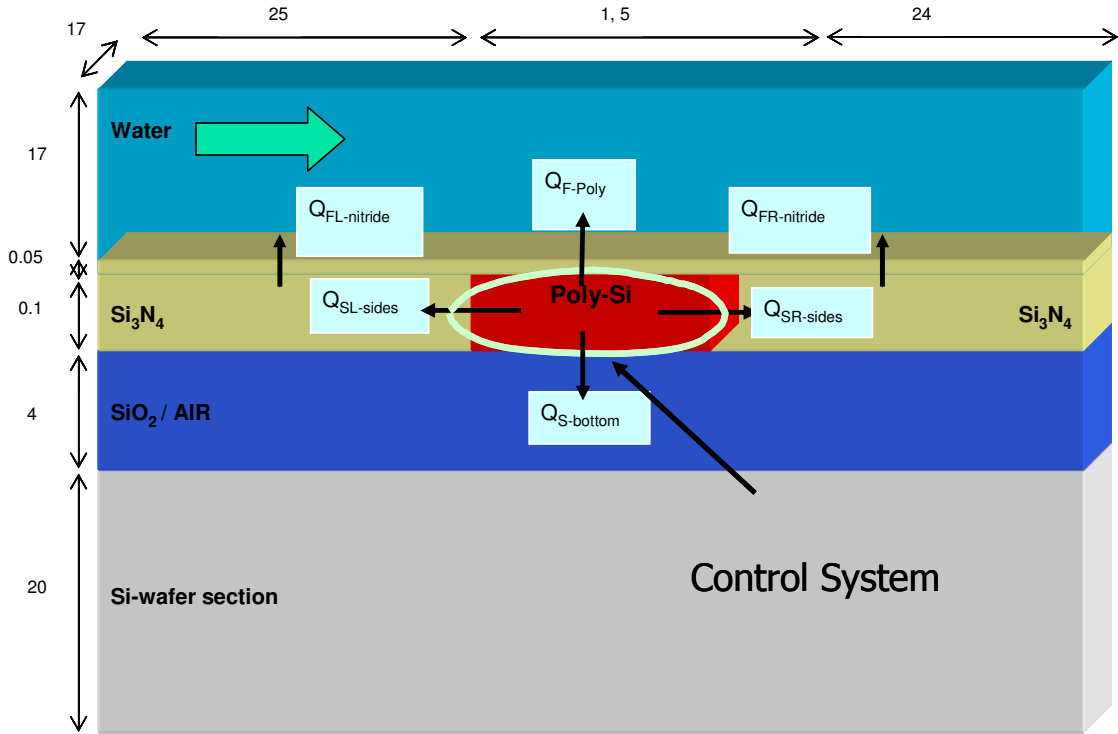
Figure 3-1 Schematic of a MEMS model (Dimensions in μm, Not To Scale)

The silicon dioxide and polysilicon thickness are varied and optimized to minimize the heat loss to the substrate. The model was also simulated by replacing silicon dioxide with air underneath the polysilicon resistor.

As shown in Figure 3-1 , consider a polysilicon resistor heated to a temperature of 310 K. The part of the heat from the polysilicon resistor will be carried away by water, Q_{F-Poly} and part of the heat will be conducted into the substrate, $Q_{SL-sides}$ + $Q_{SR-sides}$ + $Q_{S-bottom}$. Hence by control system approach, the total heat lost by the polysilicon resistor is given as,

$$Q_{Total} = Q_{F-Poly} + Q_{SL-sides} + Q_{SR-sides} + Q_{S-bottom} = Q_{F-Poly} + Q_s = \text{Power} \qquad (3-1)$$

where

$$Q_s = Q_{SL\text{-sides}} + Q_{SR\text{-sides}} + Q_{S\text{-bottom}} \qquad\qquad (3\text{-}2)$$

where $Q_{F\text{-Poly}}$ = Heat loss from polysilicon resistor to the fluid, $Q_{SL\text{-sides}}$ = Heat loss from left of the resistor to the substrate, $Q_{SR\text{-sides}}$ = Heat loss from right of the resistor to the substrate, $Q_{S\text{-bottom}}$ = Heat loss from bottom of the resistor to the fluid, and Q_S = Total heat transfer from polysilicon resistor to the substrate. Thus, a power required to keep the resistor at 310 K was calculated using control system approach.
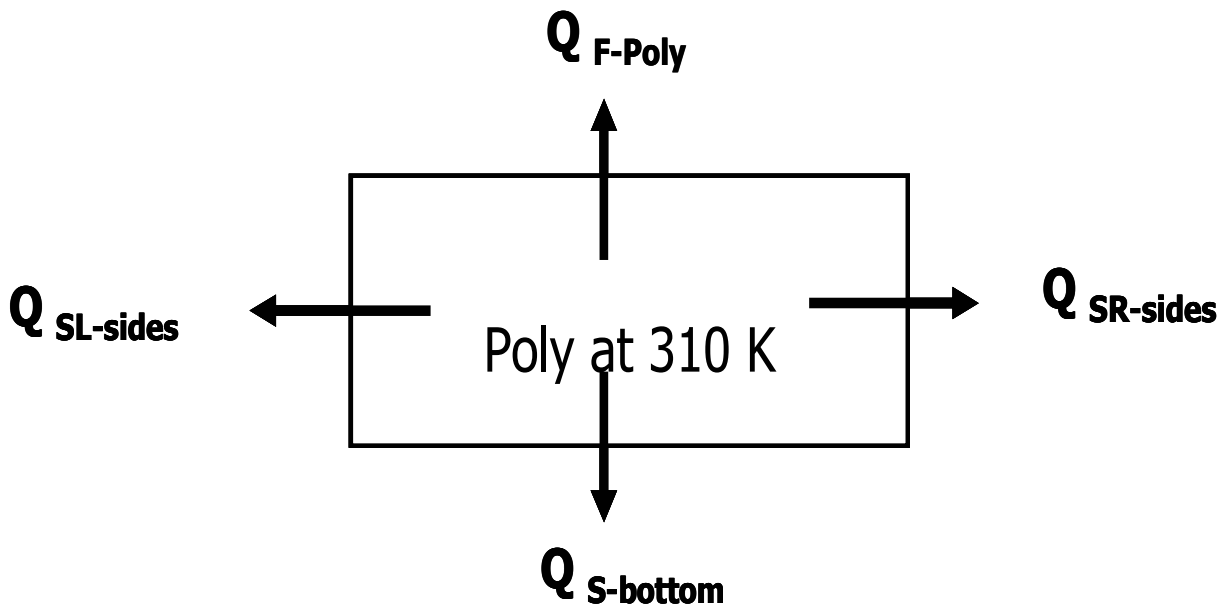

Figure 3-2 Control system approach

A control system approach (Figure 3-2) was used to determine power requirements to the thermal sensor.

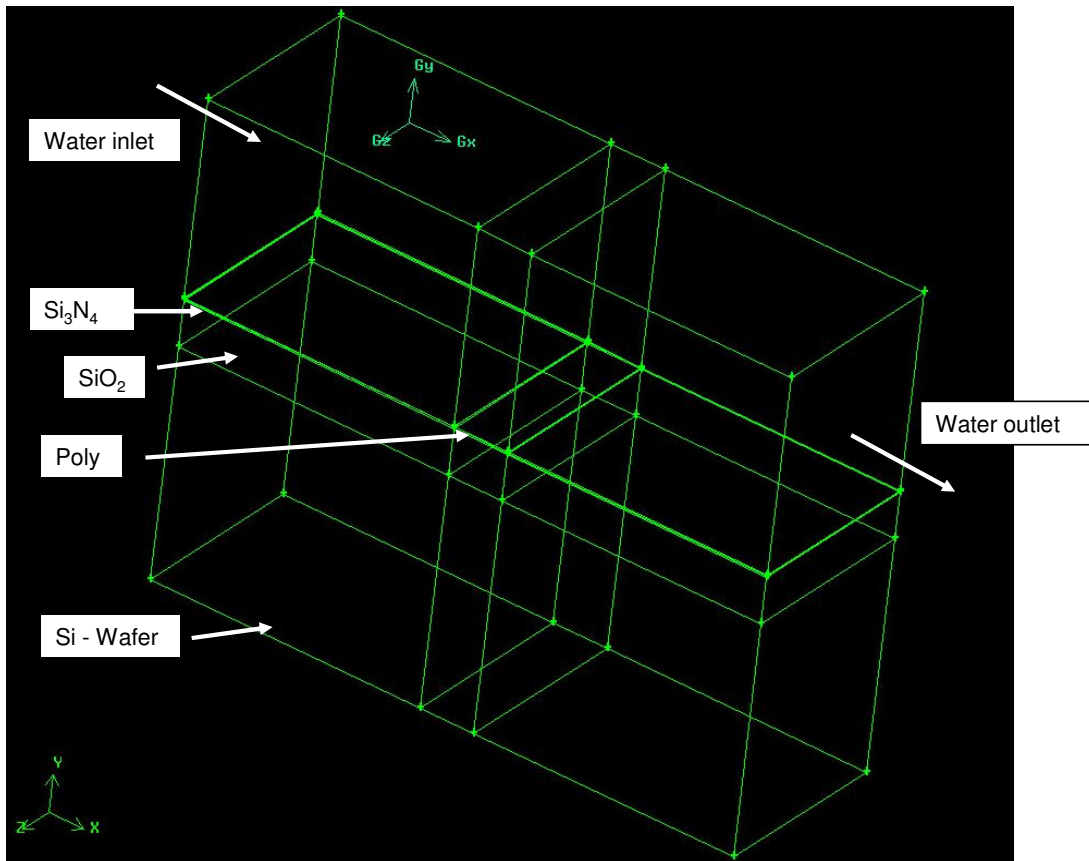Figure 3-3 shows a MEMS model created in Gambit (Preprocessor).

Figure 3-3 MEMS model created in Gambit

3.3 Calculations

This sections includes the hand calculations for water flow through microchannel of diameter = 17 µm. The volumetric flow rate, pressure drop across microchannels, wall shear stress and the entrance length had been calculated corresponding to a Re = 0.01. Some of these values served as the boundary conditions during CFD analysis of the device. This section also describes the equations needed to calculate temperature

coefficient of resistance for polysilicon resistors. It further discusses the calculations for power requirement to the sensor.

3.3.1 Calculations for volumetric flow rate and pressure drop across a microchannel

Consider a microchannel with circular cross section of diameter 17 µm with water as a working fluid. Let the length, L, of the channel be 10 mm. For a fully developed laminar flow in microchannel (Fox and McDonald, 1998),

$$\tau_{wall} = \frac{2 \times \mu^2 \times \mathrm{Re}}{\rho \times R^2} \tag{3-3}$$

where τ_{wall} is wall shear stress in Pascal, Re is Reynolds number, μ is absolute or dynamic viscosity in N-sec/m^2, ρ is density in Kg/m^3 and R is radius of the microchannel in meters. Now, for wall shear stress, assume Re = 0.01 (It will vary with temperature and flow velocity), μ = 1E-03 N-sec/m^2, ρ = 1000 Kg/m^3 and R = (17E-06/2) m. Thus,

$$\tau_{wall} = 0.276 \text{ Pa}$$

Now, average velocity is given as,

$$\overline{V} = \frac{\mathrm{Re} \times \mu}{\rho \times D} \tag{3-4}$$

$$\overline{V} = 5.882\text{E-}04 \text{ m/s}$$

This average velocity was used as an inlet boundary condition for the microchannel during the CFD analysis. Now, the volumetric flow rate is given as,

$$Q = \overline{V} \times A \tag{3-5}$$

where A is cross Sectional area of the microchannel. Thus,

$$Q = 1.335\text{E-}13 \text{ m}^3/\text{s} = 0.48 \text{ } \mu\text{l/hr}$$

Now, in a fully developed flow, the pressure gradient is constant and is given as,

$$\Delta P = \frac{128 \times Q \times \mu \times L}{\Pi \times D^4} \tag{3-6}$$

$$\Delta P = 651.24 \text{ Pa}$$

The value of Q and ΔP can be used while selecting a Syringe pump specifications for testing of the next generation device. The entrance length, L_e, is the distance down stream from the entrance to the location at which fully developed flow begins. For laminar flows,

$$\frac{L_e}{D} = 0.06 \times \text{Re} \tag{3-7}$$

$$L_e = 1.02\text{E-}08 \text{ m} = 0.0102 \text{ } \mu\text{m}$$

The flow is fully developed beyond the entrance length. Hence, the thermal hot film sensors were placed at a distance greater than the above calculated entrance length along the microchannel.

3.3.2 Thermal transfer principal for hot film sensors

The temperature change of the polysilicon resistor is measured by the change in its resistance. The resistance, R_{op}, of a semiconductor sensing element at an elevated or operating temperature, T_R, is expressed as (Liu, 1996)

$$R_{op} = R_0 \left(1 + \alpha (T_R - T_0)\right) \tag{3-8}$$

where R_0 is nominal resistance at temperature T_0, T_0 is room temperature and α is temperature coefficient of resistance. This equation was used to calculate α for

polysilicon resistors (Section 4.3). The temperature over heat ratio, α_T, is defined as the relative change of sensor temperature compared to the ambient temperature. It is given as

$$\alpha_T = \frac{T_R - T_0}{T_0} \tag{3.9}$$

The resistance over heat ratio, α_R, is defined as the relative change of sensor resistance compared to the resistance at the room temperature. It is given as

$$\alpha_R = \frac{R_{op} - R_0}{R_0} \tag{3.10}$$

Thus from equation (3.8), equation (3.9) and equation (3.10), it can be written as,

$$\alpha_R = \alpha (T_R - T_0) \tag{3.11}$$

Hence, from equation (3.9) and equation (3.11), it can be written as,

$$\alpha_R = \alpha T_0 \alpha_T \tag{3.12}$$

The thermal resistance, θ, is defined as the temperature change ΔT in a sensor element due to an input power, P. It is given as,

$$\Delta T = (T_R - T_0) \equiv \theta P \tag{3-13}$$

Thus equation (3.8) for the sensor resistance can be written as,

$$R_{op} = R_0 (1 + \alpha \theta P) \tag{3-14}$$

3.3.3 Calculations for power, voltage and current requirements to the hot film sensor

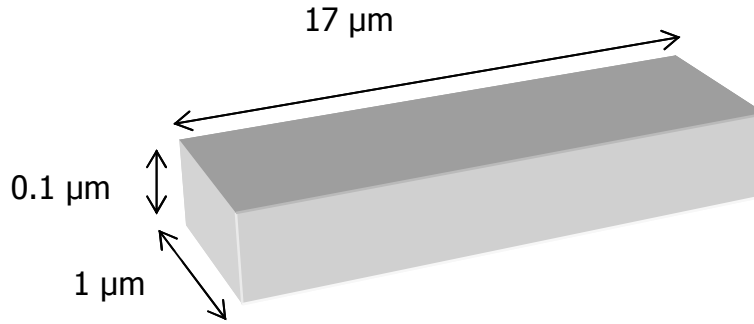Consider a thermal hot film sensor with dimensions, L = 17 μm, W = 1 μm, T = 0.1 μm as shown in Figure 3-4.

Figure 3-4 Polysilicon resistor

The measured nominal resistance, R_0 (Section 4.3) for a polysilicon resistor at 292 K (SMFL, RIT clean room temperature) is,

$$R_0 = 5010 \ \Omega$$

The operating resistance, R_{op} of Polysilicon resistor at T_R = 310 K, is given by equation 3-8. Temperature coefficient of resistance for the polysilicon resistors is calculated to be, α = 0.0003095 / ^{0}C (Section 4.3), and hence,

$$R_{op} = 5010 \ [1+0.0003095*(310-292)]$$

$$R_{op} = 5037.91 \ \Omega$$

The operating resistance of the sensor can be used while calibrating the sensor using constant temperature circuit as described in Section 6.3 for next generation device. From CFD analysis, the power, P, needed to heat the polysilicon resistor to a temperature, 310 K, is

$$Power = 0.325 \ mW \ (From \ CFD \ analysis)$$

Thus, Voltage can be given as

$$V^2 = P \times R_{op} \tag{3-15}$$

$$V = 1279.5 \text{ mV}$$

Thus, current can be given as,

$$I^2 = \frac{P}{R_{op}} \tag{3-16}$$

$$I = 0.253 \text{ mA}$$

3.3.4 Summary and Conclusions

Table 3-1 summarizes the values calculated for water flow through microchannels of diameter 17 µm.

Table 3-1 Results for water flow through microchannels

Quantity	Re	$\overline{V}$	Q	τ_{wall}	ΔP	L_e
Units	-	m/s	µl/hr	Pa	Pa	µm
Value	0.01	5.882E-04	0.48	0.276	651.24	0.0102

The average velocity, volumetric flow rate and pressure drop were calculated for Re = 0.01 flow condition. The wall shear stress values can be calculated for various flow rates and can be used for the calibration of the next generation device. Table 3-2 summarizes power requirements and operating resistance of the sensor. The power to the sensor was obtained from CFD analysis.

Table 3-2 Results for power requirements for thermal hot film sensors

Quantity	Sensor	R_0	R_{op}	α	P	V	I
Units	μm^3	Ω	Ω	$/^0C$	mW	mV	mA
Value	17*1*0.1	5010	5037.91	0.0003095	0.325	1279.5	0.253

The experimental α values was used to calculate the operating resistance of the sensor which can be used while calibrating the hot film thermal shear stress sensors.

3.4 Meshing

Mesh generation is one of the most important steps in the entire process of CFD analysis. The entire calculation in Fluent is based on the mesh and hence it is of immense importance that the mesh generated is accurate. A coarse mesh at certain places where there is a large gradient in flow properties could result in an incorrect solution and a fine mesh in places of steady flow would result in longer calculation time with no additional benefit to the problem. Hence meshing is given due attention and is an intricate process with options of different mesh styles, mesh elements as well as quality of mesh.

Figure 3-5 shows a model with a mesh created using Gambit. The hex elements with type 'map' and the interval size = 5E-05 cm was used. As it can be seen in Figure 3-5, a fine mesh scheme was used to increase the accuracy of the analysis.
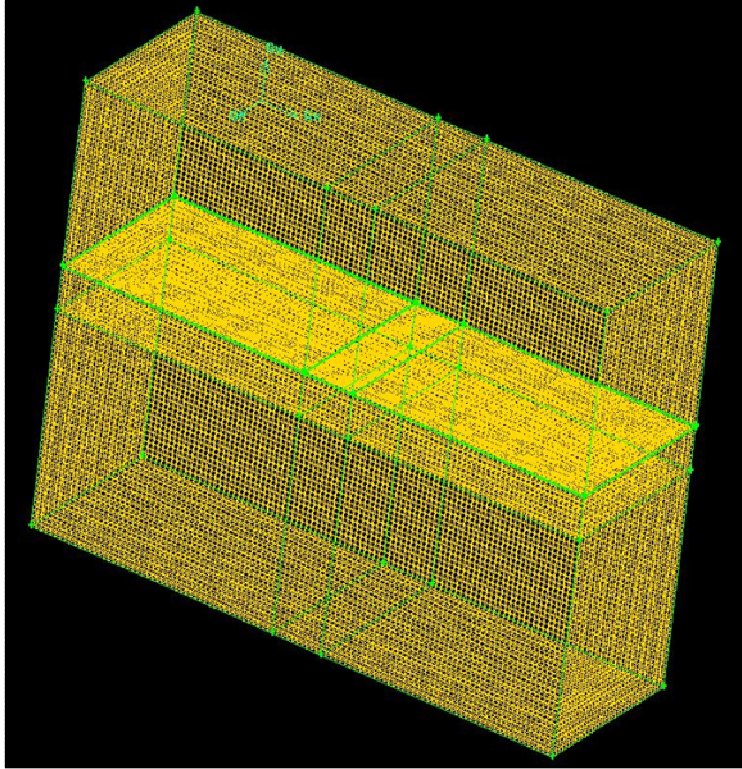
Figure 3-5 MEMS model with a hex type mesh elements

3.5 Boundary Conditions

The following were the boundary conditions applied to the MEMS model in Fluent: Heat generated in polysilicon resistor i.e. E_g = 0 W/m3 (Source term). The polysilicon resistor temperature (T_R = 310 K) ,10 ^{0} K higher than the room temperature (300 K) was chosen. This was because the viscosity of water changes by ~20% with the temperature change of 10 K (Fox, 1998). Velocity of water at the inlet of the microchannel of 17 * 17 μm^2 was calculated to be 5.884E-04 m/s (Section 3.3.1). The velocity value was corresponding to a Re = 0.01. Re = 0.01 is commonly observed for blood flow in arteriole (Noren, 1999). Pressure at the outlet of the microchannel was considered to be atmospheric pressure (P_{atm}). All the outer surfaces were considered to be insulated.

3.6 Optimization of Sensor Dimensions using Fluent Results

3.6.1 Optimization of polysilicon resistor thickness

The polysilicon resistors (L = 5 µm, W = 17 µm) **with thickness 0.1 µm, 0.2 µm and 0.3 µm w**ere **modeled and the corresponding heat loss to the substrates, Q**$_S$ **was obtained.** The SiO$_2$ thickness **was held constant at 4 µm.** The r**esults are plotted in Figure 3-**6**.** As expected, heat loss to substrate with polysilicon thickness 0.1 µm was lowest ($Q_S \propto \dfrac{1}{t_{poly}}$). Hence, the polysilicon resistor of thickness 0.1 µm was decided for the final device. The thickness value lower than 0.1 µm could not be considered as it was not possible to deposit polysilicon < 0.1 µm using LPCVD at SMFL, RIT.
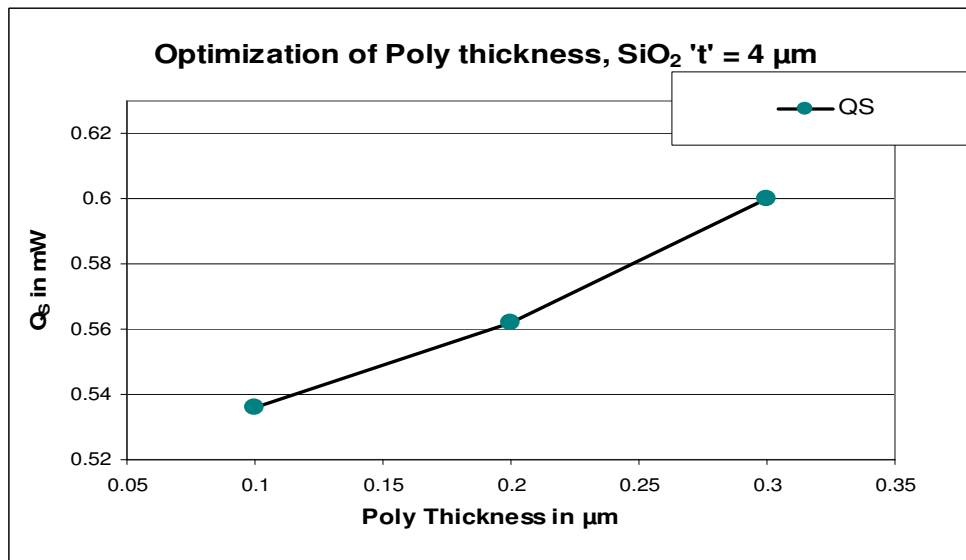

Figure 3-6 Optimization of polysilicon resistor thickness

3.6.2 Optimization of silicon dioxide thickness

The silicon dioxide thickness was varied from 0.25 µm to 4.75 µm and the corresponding heat loss to the substrates was obtained. From Figure 3-7, it was observed that with the silicon dioxide thickness 4.75 µm, the heat loss to the substrate was lowest. This was the expected result as the heat conducted is inversely proportional to the thickness ($Q_S \propto \dfrac{1}{t_{SiO_2}}$). The silicon dioxide was decided to grow underneath the polysilicon resistors because of its low thermal conductivity, K_{SiO2} = 1.3 W/m-K. These led to the reduction in heat loss to the substrate and hence increase in the sensitivity of thermal hot film shear stress sensors (Section 2.3.2).
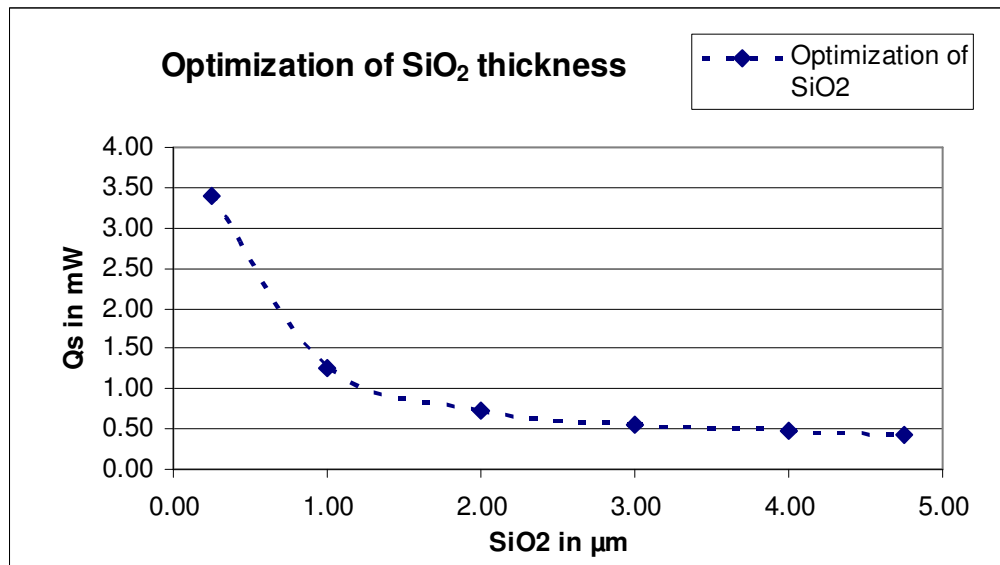

Figure 3-7 Optimization of silicon dioxide thickness

It was decided to grow silicon dioxide thermally using Bruce Furnace at SMFL, RIT. The time required to grow 4 µm of silicon dioxide was ~ 36 hrs. Hence, silicon dioxide of thickness 4 µm was decided to grow for the thermal shear stress sensors.

3.6.3 Optimization of air pocket size

The heat loss to the substrate was obtained by replacing silicon dioxide with air. The air pocket thickness was varied from 0.25 µm to 4.75 µm and the corresponding heat loss to the substrates was obtained. From Figure 3-8, it was observed that the heat loss to the substrate was reduced with increasing thickness of air pocket size. It was expected as
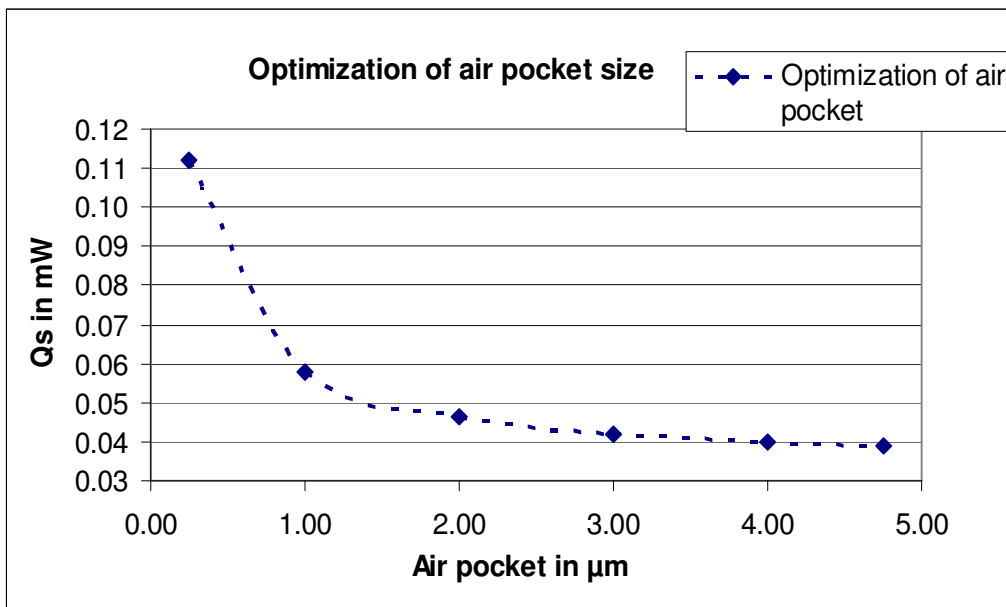
$$Q_S \propto \frac{1}{t_{air}}.$$

Figure 3-8 Optimization of air pocket size

3.6.4 Silicon dioxide verses air pocket

Heat loss to the substrate with silicon dioxide and air underneath polysilicon resistor was compared. It was expected to obtain less heat loss to the substrate with air as this is the latest design trend in building hot film thermal shear stress sensors (Huang,1995). From Figure 3-9, it was observed that the heat loss to the substrate with silicon dioxide underneath the polysilicon resistors was ~10 times greater, in comparison with air pocket.
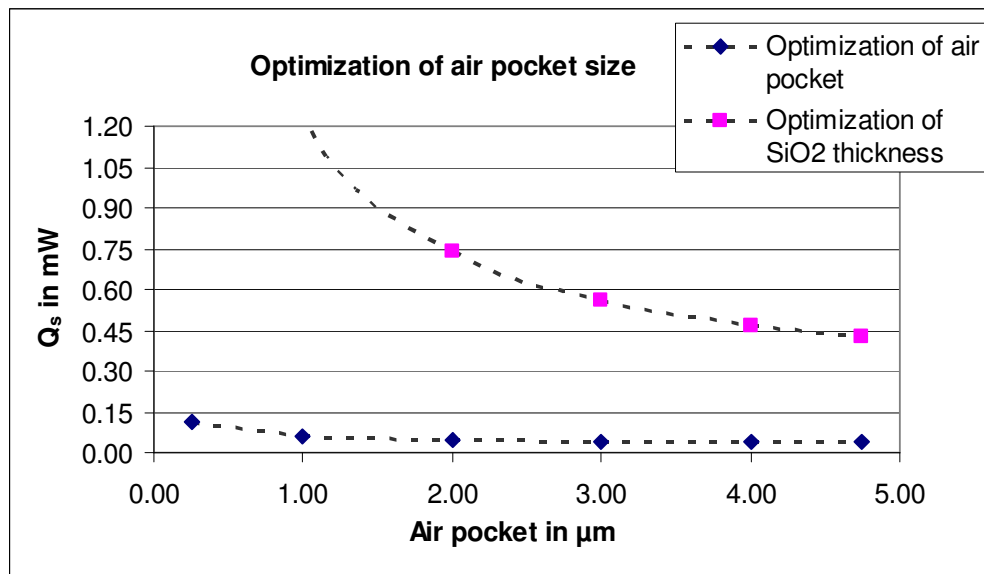

Figure 3-9 Silicon dioxide VS air pocket size

This was because the conductivity of air is 0.0242 W / m-K whereas that of silicon dioxide is 1.3 W / m-K. It was decided not to use air as it was easy to grow thermal silicon dioxide underneath the polysilicon resistors at SMFL, RIT. The

fabrication of the device would have been much more challenging with the use of air pocket.

3.6.5 Summary and Conclusions

The Fluent model of microchannel integrated with hot film shear stress sensors was analyzed and optimized using a CFD approach. It was decided to fabricate the sensors with polysilicon resistor thickness = 0.1 µm and SiO_2 thickness = 0.4 µm. The power to heat polysilicon resistor at 310 K was obtained to be 0.325 mW using control system approach. Thus, CFD served as a tool to optimize the sensor dimensions and to obtain power requirements to the sensor.

3.7 Effects at Higher Reynolds' Numbers

Figure 3-10 illustrates a thermal hot film sensor (polysilicon resistor) heated at 310 K. Water is flowing from left to right as shown in figure. The heat lost to the fluid as well as to the substrate can be seen.
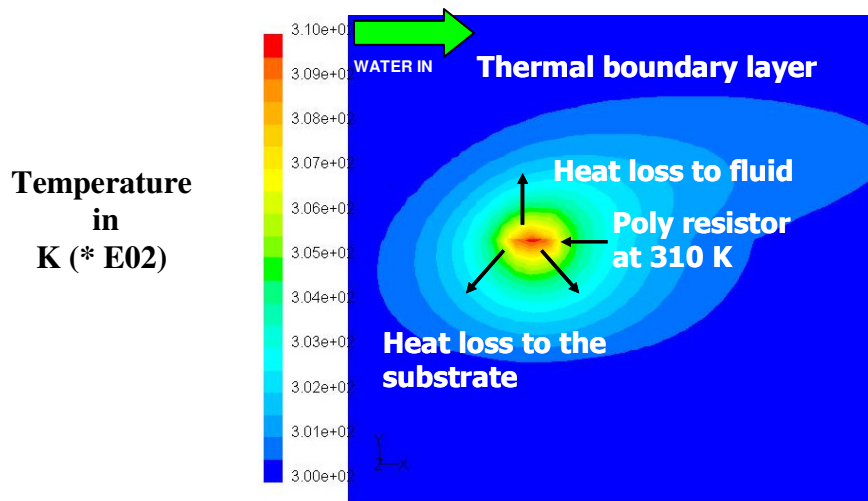

Figure 3-100 Heat losses from a polysilicon resistor

Figure 3-11 shows the effect on the thermal boundary layer with increasing Reynolds number (Re).
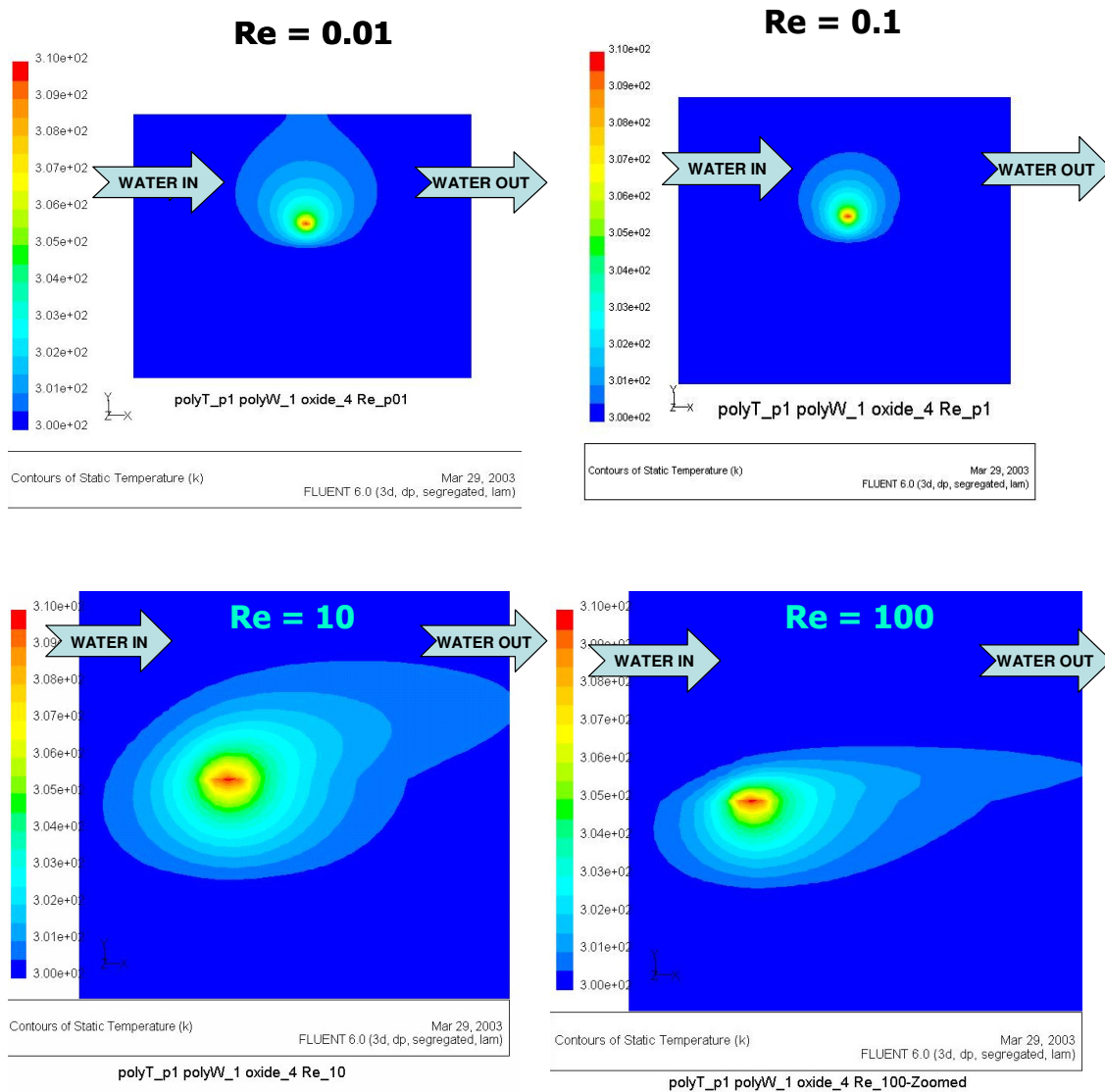

Figure 3-111 Effects of Reynolds number on thermal boundary layer

The first simulation was done with Re=0.01 as this is the common in vivo value for blood flow in arteriole (Noren, 1999). It can be observed from Figure 3-11, for Re = 0.01 and Re = 0.1, the heat from the sensor was conducted into water and not carried away by water. This was in contradiction with the assumptions 3 and 4 described in

Section 2.3.2. It was observed that with Re = 10 and Re = 100, the heat from sensor was carried away by water. The thickness of the thermal boundary layer was also decreased with Re = 10 and Re = 100. Hence it was decided to test the device for $Re \geq 10$.

Chapter 4

Fabrication-Micromachined Thermal Shear Stress Sensors integrated with Microchannels

This chapter discusses the fabrication process for the device. The mask layouts were created using Mentorgraphics software tool. Using MEBES III e-beam lithography, the masks were fabricated at RIT SMFL facility. There were total four mask levels present in the fabrications. The microchannels integrated with thermal hot film sensors were fabricated in house at SMFL, RIT facility.

4.1. CAD layouts using Mentorgraphics Tool and Mask making

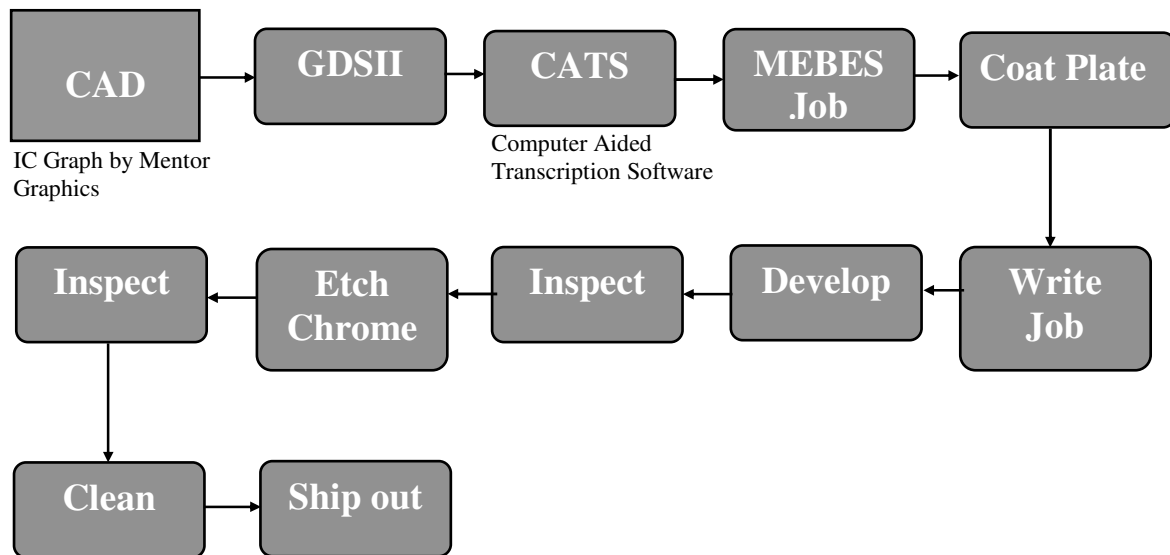Figure 4-1 shows a process flow from creating a IC layout to the fabrication of the mask.

Figure 4-1 Steps during the mask fabrication

The important steps during the mask fabrication are as follows: Using Mentor Graphics Design Tools layout the device layers. Save the layout as a GDSII file format. The GDSII format is then transferred to the CATS system for fracturing. (Fracturing means the layer to be fractured is as a dark or light field image as shown in Figure 4-2). Finally save the file on magnetic tape to transfer to the MEBES e-beam lithography tool. Figure 4-3 shows a GCA stepper reticle schematic at RIT. The fiducial marks (clear or dark) as shown in Figure 4-3 are on the mask and used to align the mask to the stepper.
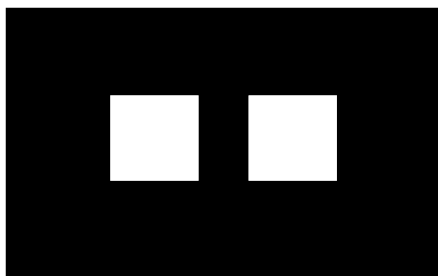
Dark Field: Black is chrome, White is Quartz.
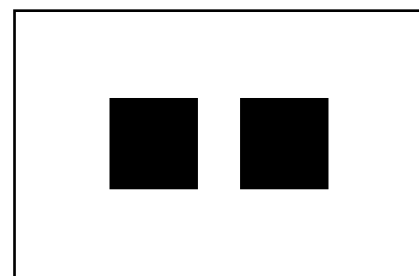
Light Field: Black is chrome, White is Quartz.

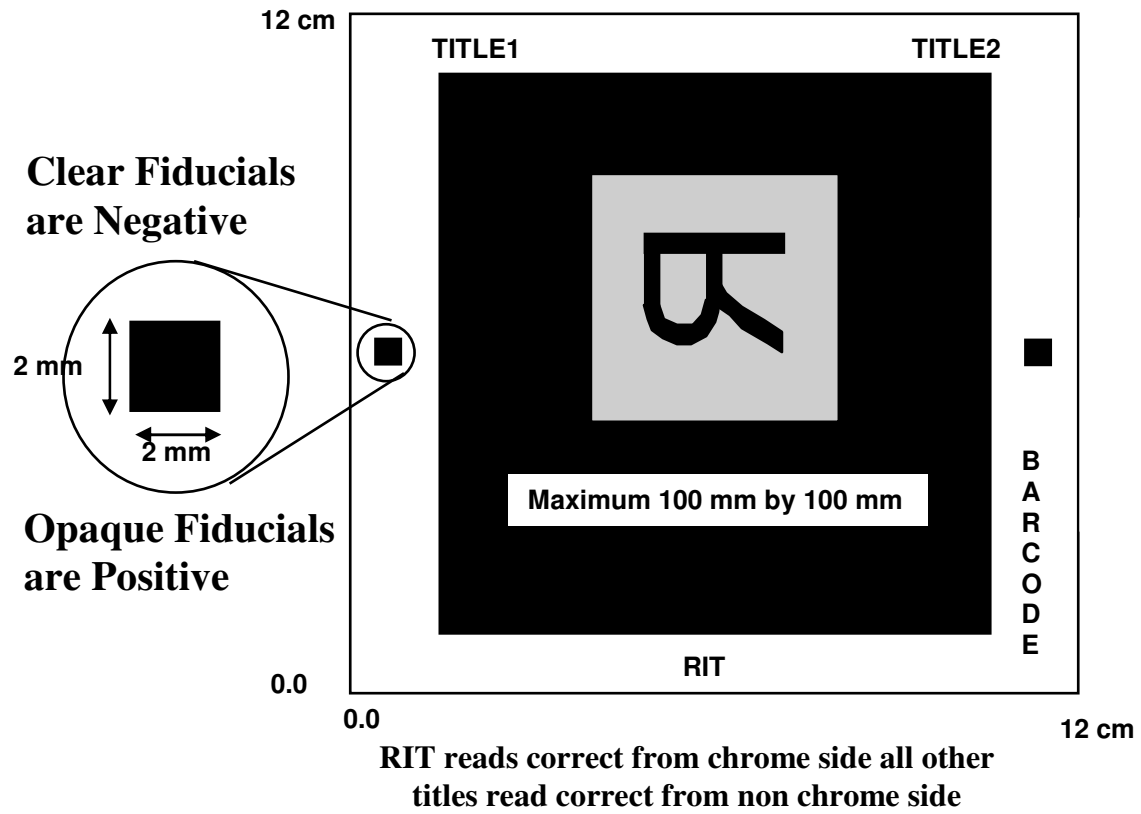**Figure 4-2 Dark and light field images on the mask**

Figure 4-3 GCA stepper reticle at RIT

Figure 4-4 shows alignment key for GCA stepper. Alignment marks are on the wafer and used to align the mask to the stepper. Table 4-1 lists four mask levels created using the mentorgraphics tool.
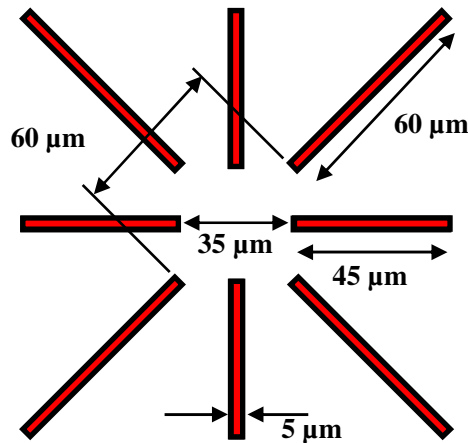

Figure 4-4 GCA alignment key

Table 4-1 Mask levels for the device

Level	Mask Description	Field Type
1	Pattern nitride to define resistors	Dark
2	Contact cuts	Dark
3	Metal	Clear
4	Microchannels	Dark

Figure 4-5 shows layout of polysilicon resistors created using Mentorgraphics tool. Figure 4-6 shows layout of contact cuts created using Mentorgraphics tool. Figure 4-7 shows layout of metal created using Mentorgraphics tool. Figure 4-8 shows layout of microchannel created using Mentorgraphics tool. Figure 4-9 shows layout of the entire chip with all lithography levels overlapping. Figure 4-10 shows part of the chip layout with polysilicon resistors. It can be seen that three resistors are aligned with microchannel before bifurcation. Also three resistors on each branch of the microchannel after bifurcation are present. Using MEBES III e-beam lithography, all masks were fabricated at RIT SMFL facility.
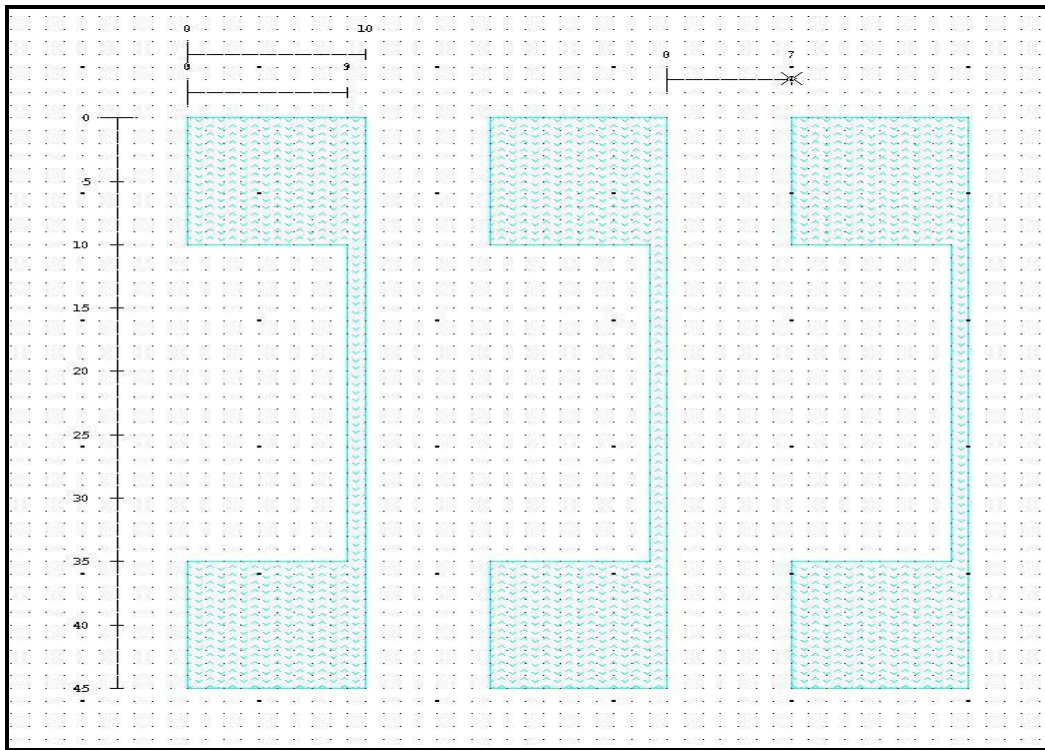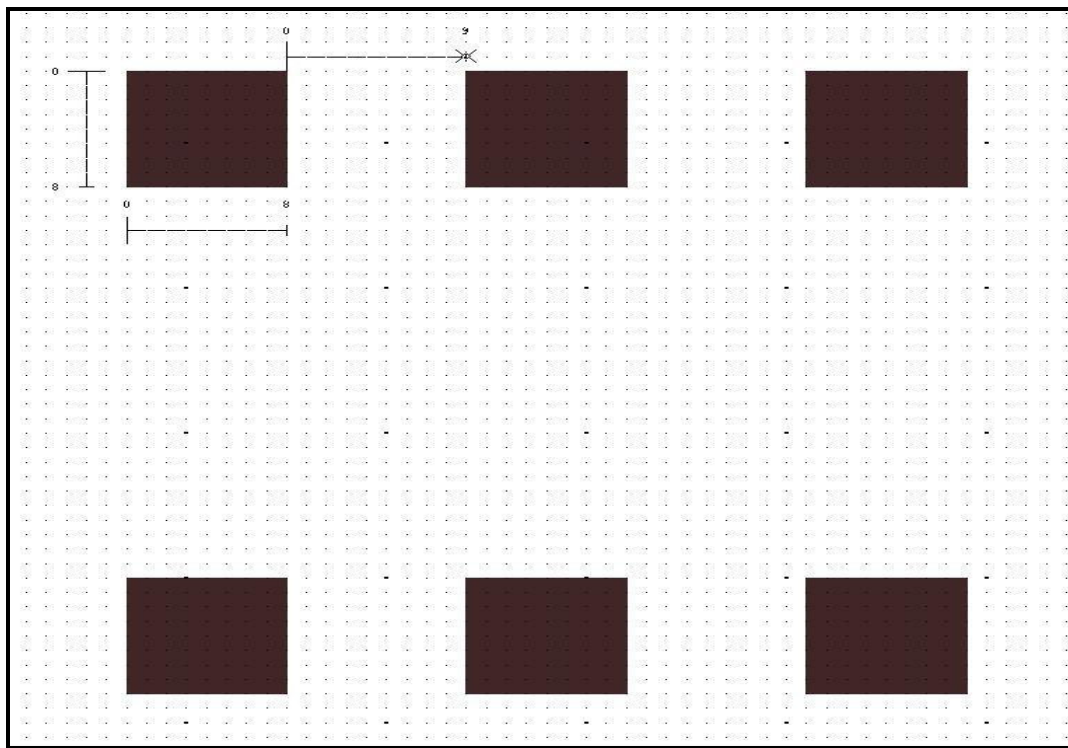
Figure 4-5 Level 1: Polysilicon resistors (3)

Figure 4-6 Level 2: Contact cuts
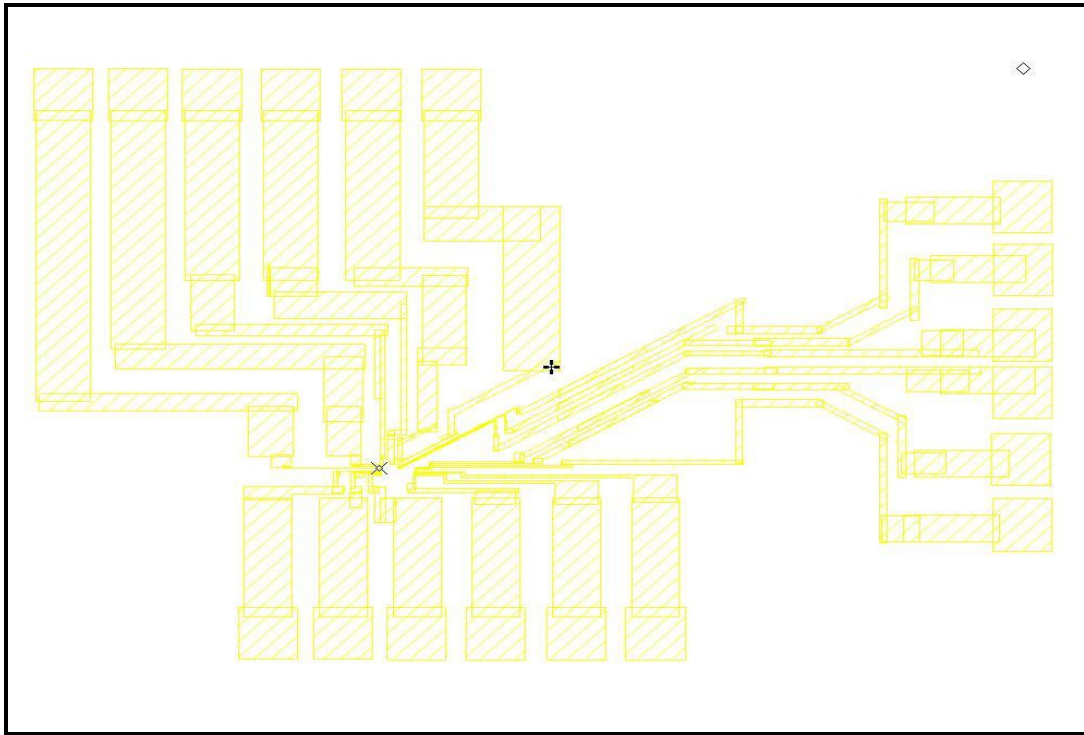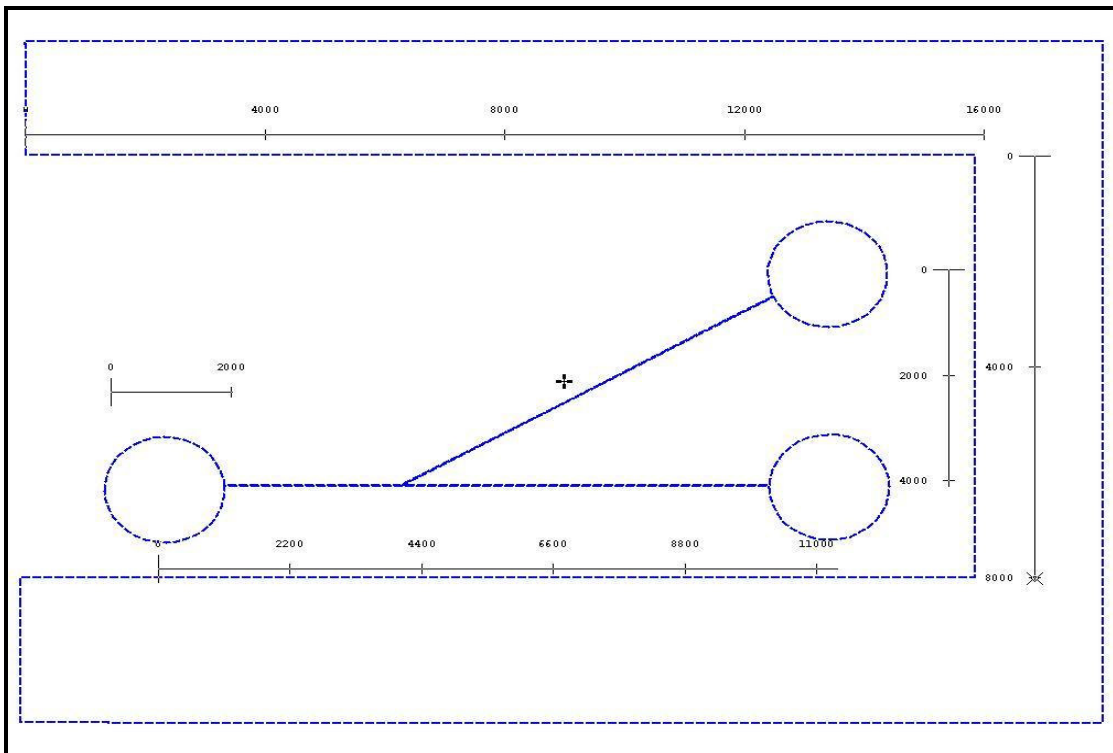
Figure 4-7 Level 3: Metal

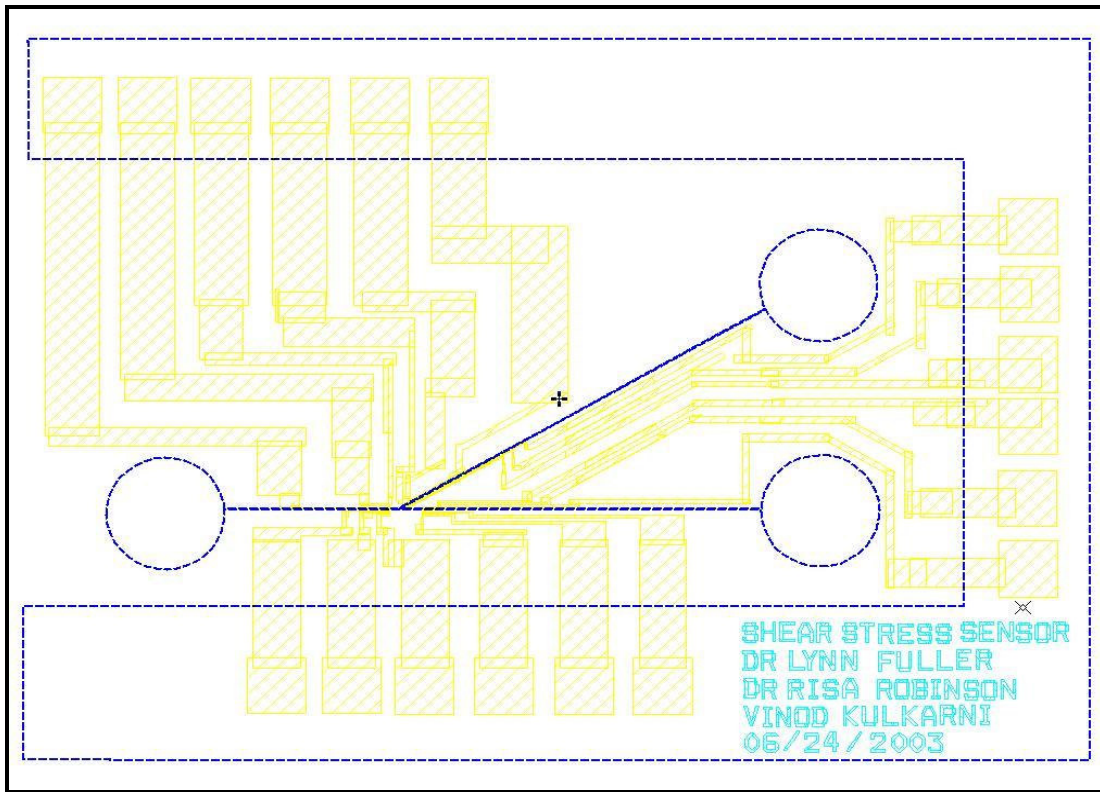**Figure 4-8 Level 4: Microchannel with 30 ^{0} bifurcation**

Figure 4-9 Layout of the entire chip with all levels overlapping
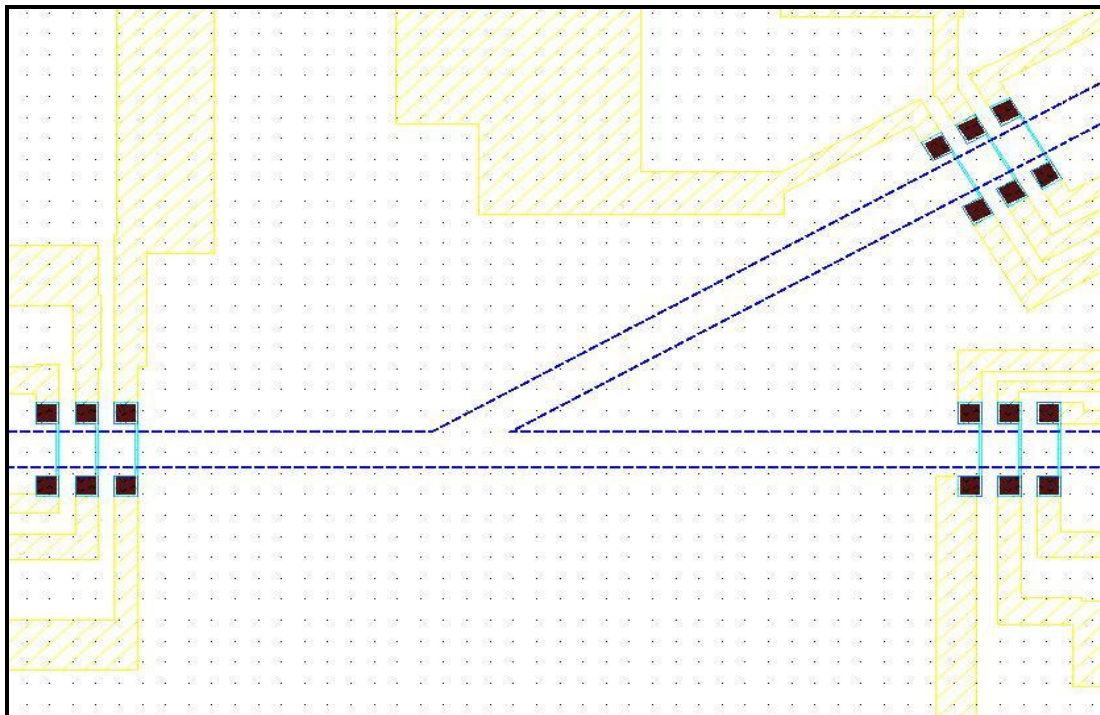

Figure 4-10 Layout showing resistors aligned with microchannel

4.2. Fabrication Steps and results

This section describes the fabrication steps, schematics and pictures of the device at major fabrication steps and results. Table 4-2 lists all the fabrication steps with a brief process description. Table 4-3 lists various values obtained during the fabrication of the device. The schematic of major steps during fabrication are shown in Figures 4-11, 4-12, 4-13, 4-14 and 4-15. Figure 4-16 shows polysilicon resistors after step 15 in device fabrication. Figure 4-17 shows polysilicon resistors aligned with contact cuts after step 21 in device fabrication. Figure 4-18 shows thermal hot film shear stress sensors after step 26 in device fabrication. Figure 4-19 shows microchannels aligned with thermal hot film shear stress sensors after step 32 in device fabrication. The microscope slide as shown in Figure 4-20 was used to cover the microchannels. Using the dental drill and drummel tool, three holes were drilled in the microscope slide. The dental drills were the diamond drills made by Star Dental, Division of de DEN-TAL-EZ, INC., Lancaster, PA 17601 and distributed by Johnson & Lund Co., Inc. 3495 Winton Place, Bldg D., Rochester, NY 14623, (585) 475 – 0160. Bit numbers AT39LP and D3P were used to drill holes.

Table 4-2 Device fabrication steps

Steps	Process Description
1	Scribe identification using diamond tip pen on 4" bare silicon P-type wafers
2	Standard RCA clean
3	Grow 40000 A^0 thermal oxide at $1100\,^0C$ in wet O_2 for 35 hrs
4	Deposit 1000 A^0 LPCVD Nitride at $810\,^0C$ in SiH_2Cl_2/NH_3 for 20 min
5	**Litho Level 1: Pattern nitride to define resistors**
6	Dry etch nitride using SF_6 for 2 min 20 sec (Timed etch)

Steps	Process Description
7	Resist Strip in O_2 plasma
8	Standard RCA clean
9	Deposit 2000 A^0 LPCVD polysilicon at 610^0 C in SiH_4 for 33 min 20 sec
10	Emulsitone N250 Spin on Glass at 3000 rpm for 30 sec
11	Bake Spin on Galss at 200^0 C for 15 min in oven
12	Dope polysilicon at 1000^0 C in N_2 for 15 min
13	Etch Phosphorus Glass in BOE for 2 min, Rinse and spin dry
14	Measure sheet resistance using 4 point probe method
15	CMP of polysilicon - 6 min/wafer, CMP clean and standard RCA clean
16	Grow 250 A^0 thermal oxide at 900^0 C in dry O_2 for 50 min
17	Deposit 500 A^0 LPCVD Nitride at 810^0 C in SiH_2Cl_2/NH_3 for 11 min
18	**Litho Level 2: Contact cuts**
19	Dry etch nitride using SF_6 for 50 sec (Timed etch)
20	Etch oxide in BOE for 20 sec, Rinse and spin dry
21	Resist Strip in O_2 plasma
22	Deposit Al/Si by sputtering for 40 min
23	**Litho Level 3: Pattern metal**
24	Etch Al/Si in wet etchants at 50^0 C for 3 min
25	Resist Strip in O_2 plasma
26	Sintering in H_2/N_2 at 450^0 C for 30 min
27	**Litho Level 4: Microchannels in positive thick photoresist**
28	Priming wafers using HMDS at 4000 rpm for 1 min
29	Coat AZ PLP 100 XT resist at 2000 rpm for 45 sec to obtain ~17 µm thickness
30	Soft bake at 115^0 C for 3 min
31	Expose using GCA stepper for 15 sec (~ 3600 mj/cm^2)
32	Develop in CD-26 for 12 min or till clear
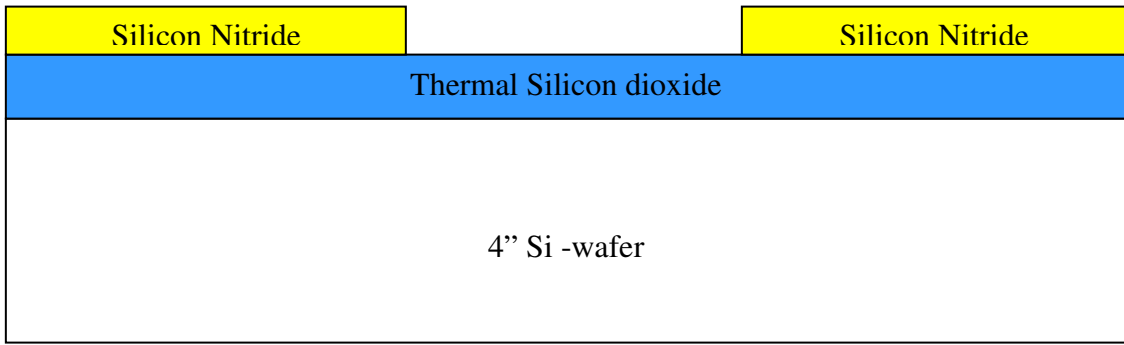
Figure 4-11 Pattern nitride to define resistors (Lithography step 1)
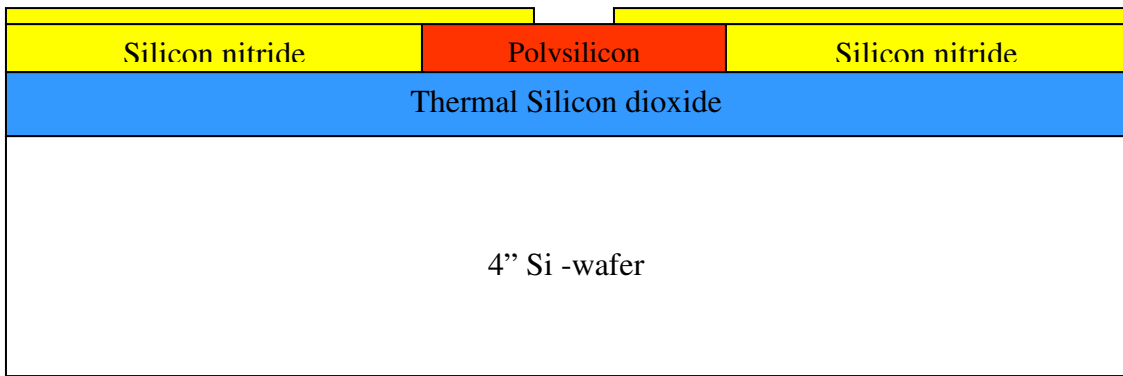
Figure 4-12 Fabrication of contact cuts in nitride (Lithography step 2)
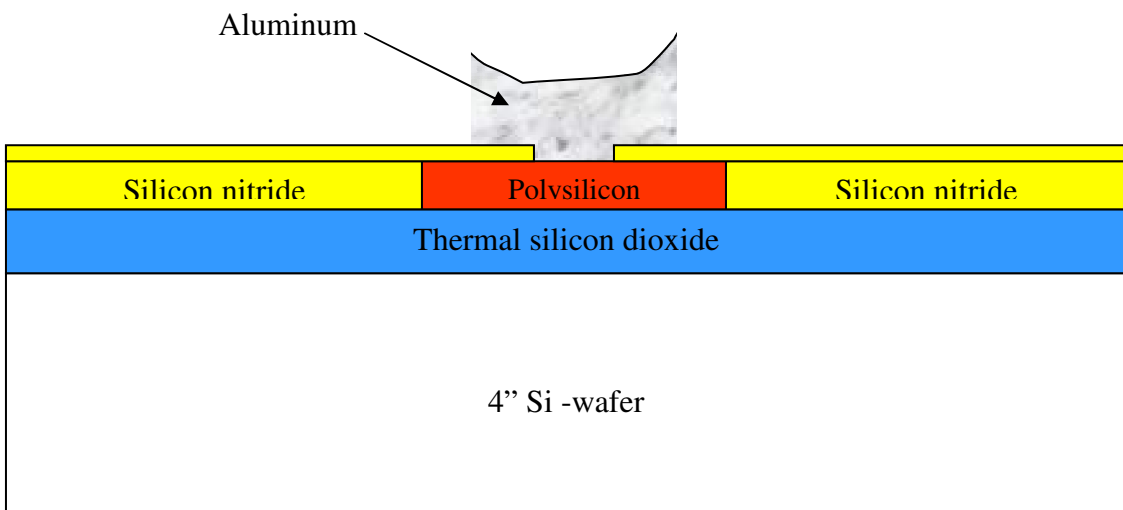
Figure 4-13 Pattern aluminum (Lithography step 3)
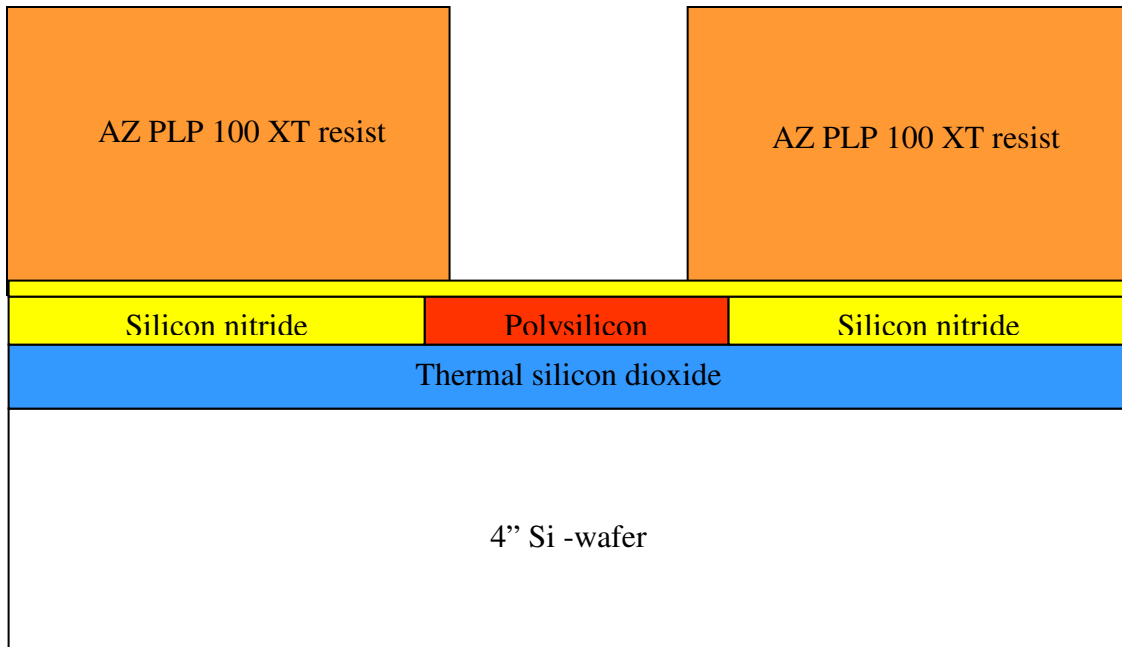
Figure 4-14 Microchannels using AZ 100 positive photoresist (Lithography step 4)
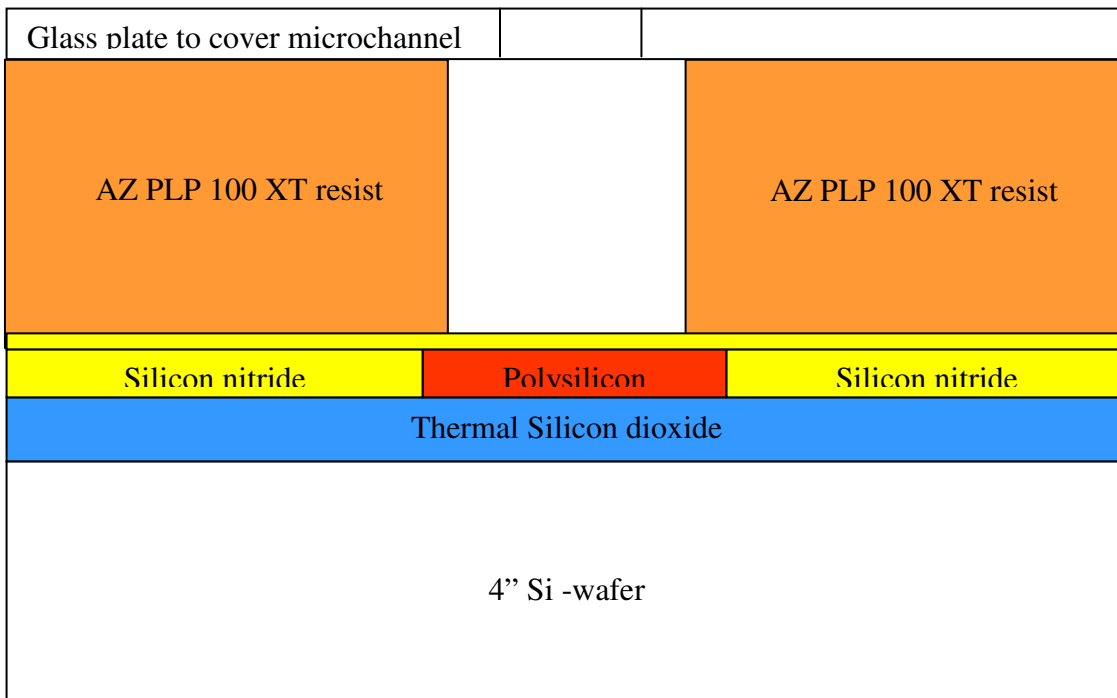
Figure 4-15 Final device showing microchannels covered with glass plate
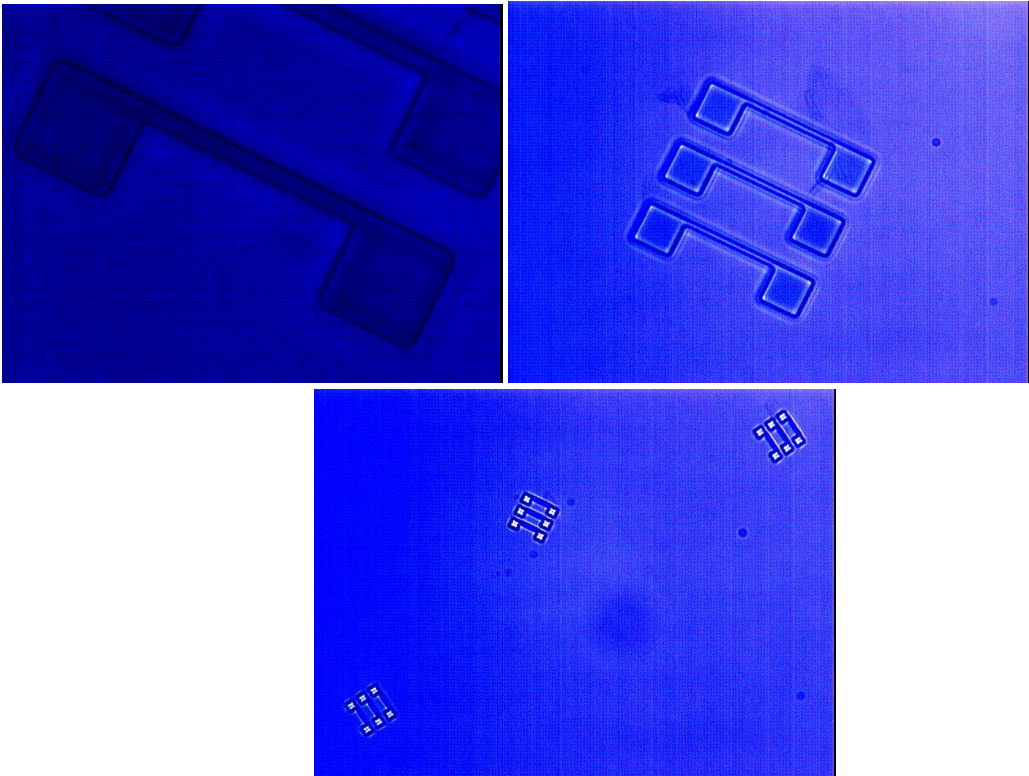
Figure 4-16 Polysilicon resistors
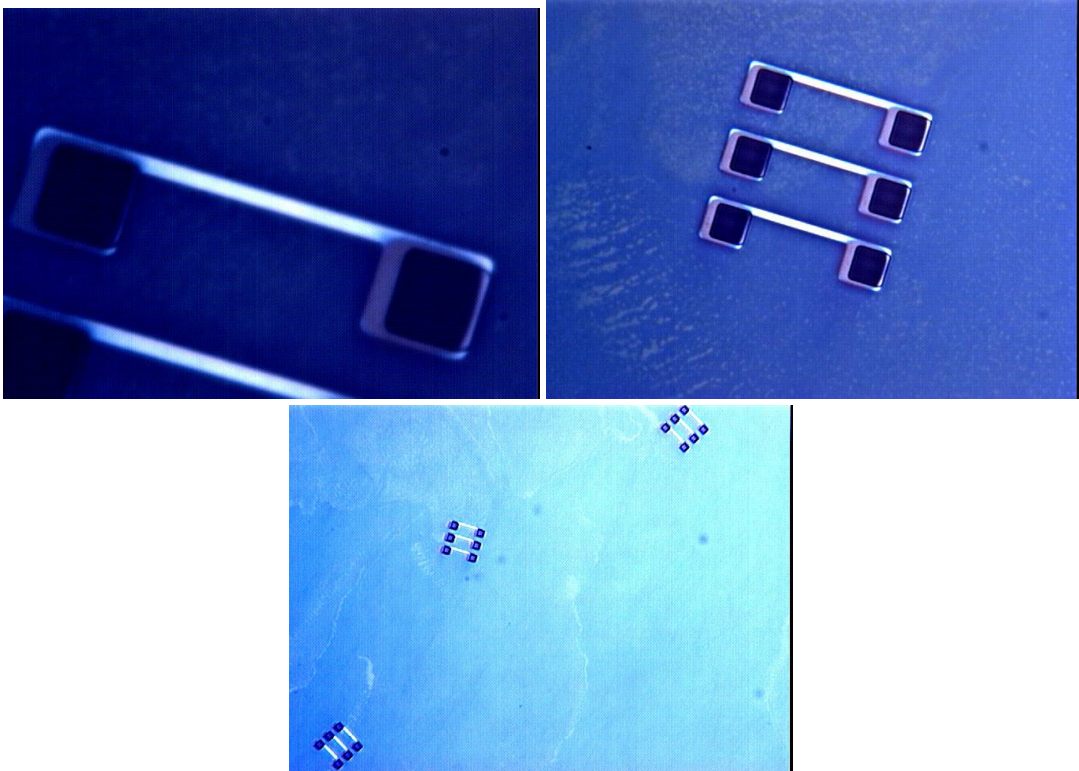
Figure 4-17 Polysilicon resistors aligned with contact cuts
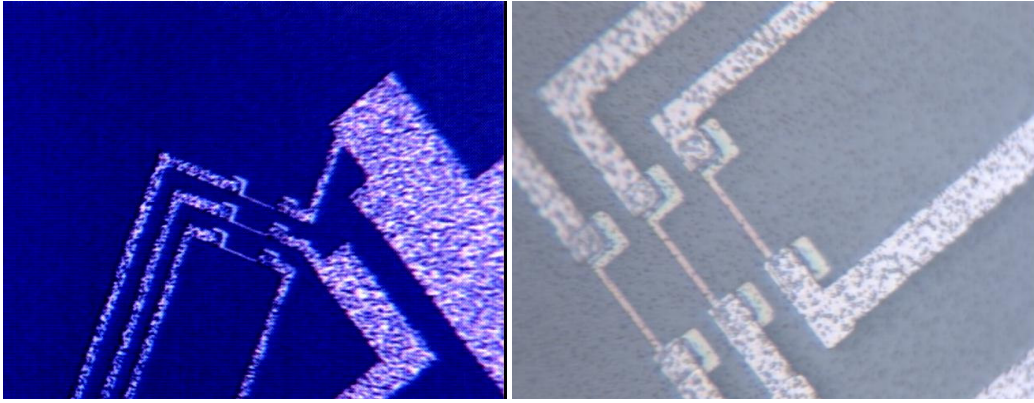
Figure 4-18 Flush mounted thermal hot film shear stress sensors
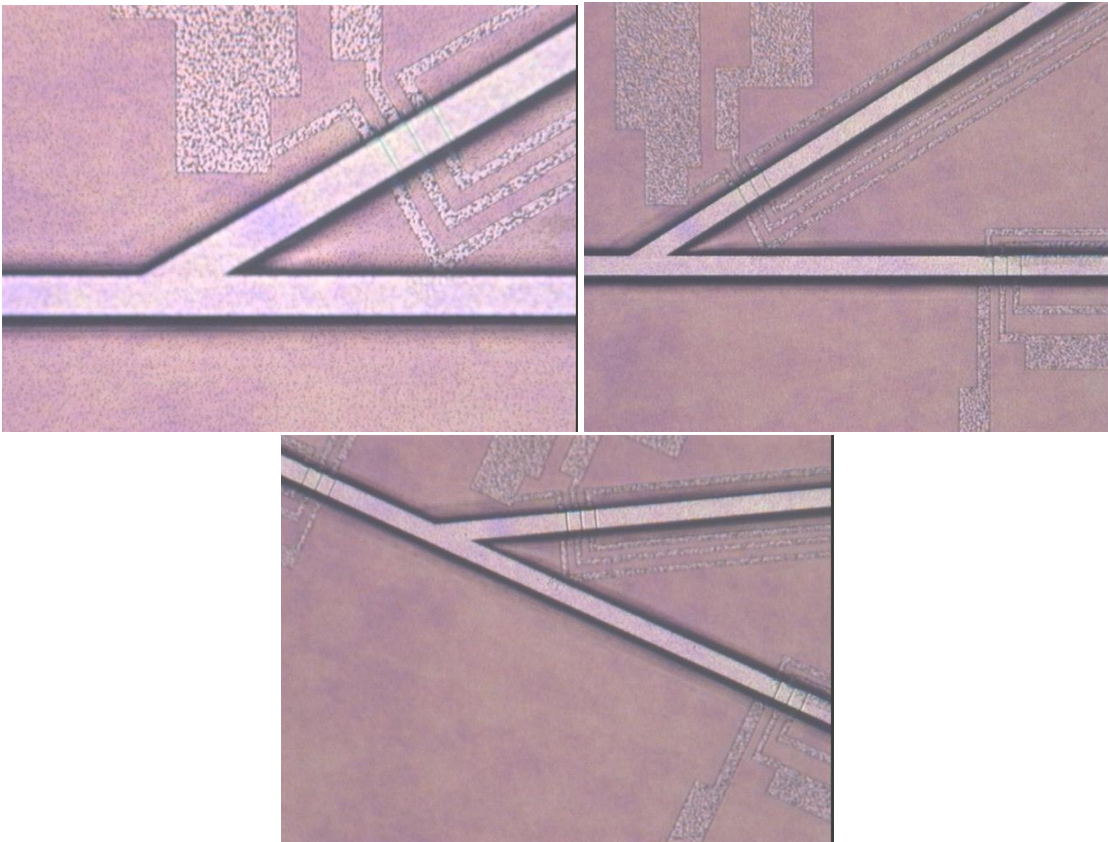
Figure 4-19 Microchannel with 30 ^{0} bifurcation angle aligned with resistors
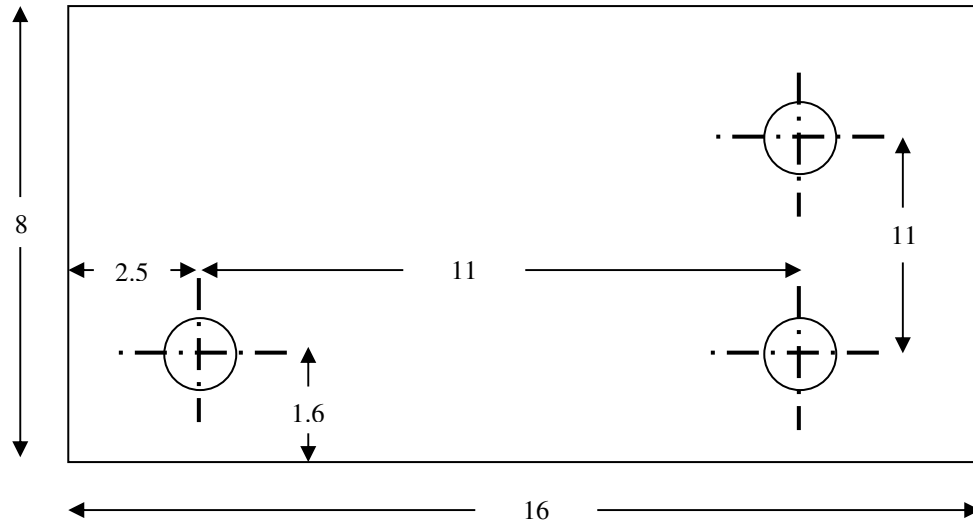
Figure 4-20 Glass plate to cover microchannels (Dimensions in mm)

Table 4-3 Fabrication results

Fabrication Step	Quantity	Results
3	Silicon dioxide thickness	37600 A^0
4	Silicon nitride thickness	1176 A^0
9	Polysilicon thickness	2300 A^0
14	Polysilicon sheet resistance	58.25 Ω / square
22	Aluminum thickness	7000 A^0
29	AZ 100 resist thickness	16.5 μm

4.3. Measurement: Temperature Coefficient of Resistance

This section describes the calculation of experimental temperature coefficient of resistance for the fabricated polysilicon resistors. The resistance, R_{op}, of a semiconductor sensing element at an elevated or operating temperature, T_R, is expressed earlier as equation 3-8 (Liu, 1996),

$$R_{op} = R_0 \left(1 + \alpha (T_R - T_0)\right) \tag{4-1}$$

where R_0 is nominal resistance at temperature T_0, T_0 is room temperature = 21 ^{0}C, α is temperature coefficient of resistance in $/ {}^0$C. Thus, rewriting the temperature coefficient of resistance,

$$\alpha = \frac{\left(R_{op} - R_0\right)}{R_0 \times (T_R - T_0)} \tag{4-2}$$

Table 4-2 lists three different resistors heated at different temperatures with their corresponding resistances.   Figure 4-21 shows a plot of measured resistance versus temperature for three different resistors. Hence, from Figure 4-21,

$$slope = \frac{\left(R_{op} - R_0\right)}{(T_R - T_0)} = 1.5506 \ \Omega / {}^0\text{C}.$$

Therefore,

$$\alpha = \frac{\left(R_{op} - R_0\right)}{R_0 \times (T_R - T_0)} = 1.5506 / 5.01\text{E}3 = 0.0003095 / {}^0\text{C} = 0.03095 \ \% / {}^0\text{C}$$

This experimental temperature coefficient of resistance, α, is used to calculate the operating resistance , R_{op}, of polysilicon resistors as described in section 3.3.3.

Table 4-4 TCR measurement

Temp in C	Resistance in ohms measured using multimeter		
	R1	R2	R3
21	5.01E+03	5.01E+03	5.01E+03
35	5.04E+03	5.17E+03	5.17E+03
45	5.06E+03	5.19E+03	5.19E+03
55	5.06E+03	5.20E+03	5.20E+03
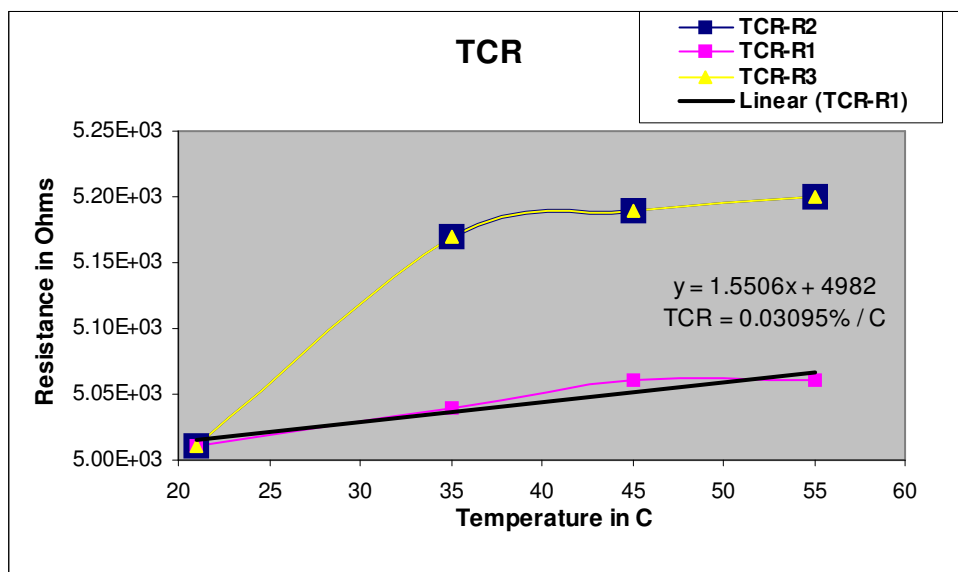
Figure 4-21 TCR measurement

Chapter 5

Testing

5.1. Device Setup and testing results

Shown in Figure 5-1 is an experimental setup at RIT Microelectronic Engineering test lab. Figure 5-2 shows a schematic of the experimental set up.
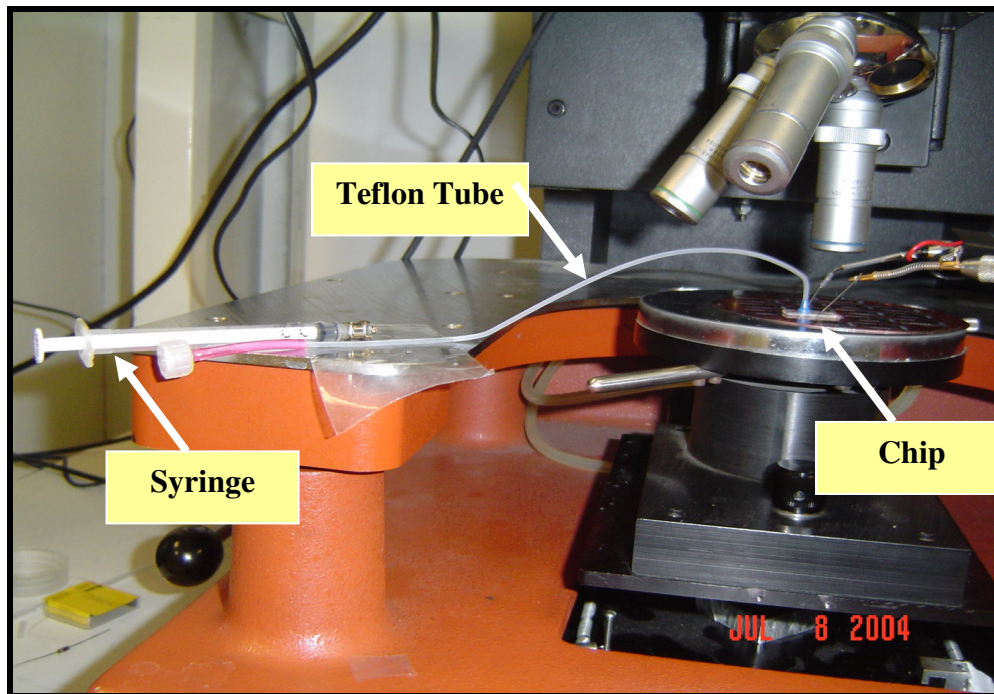
Figure 5-1 Experimental Test Setup
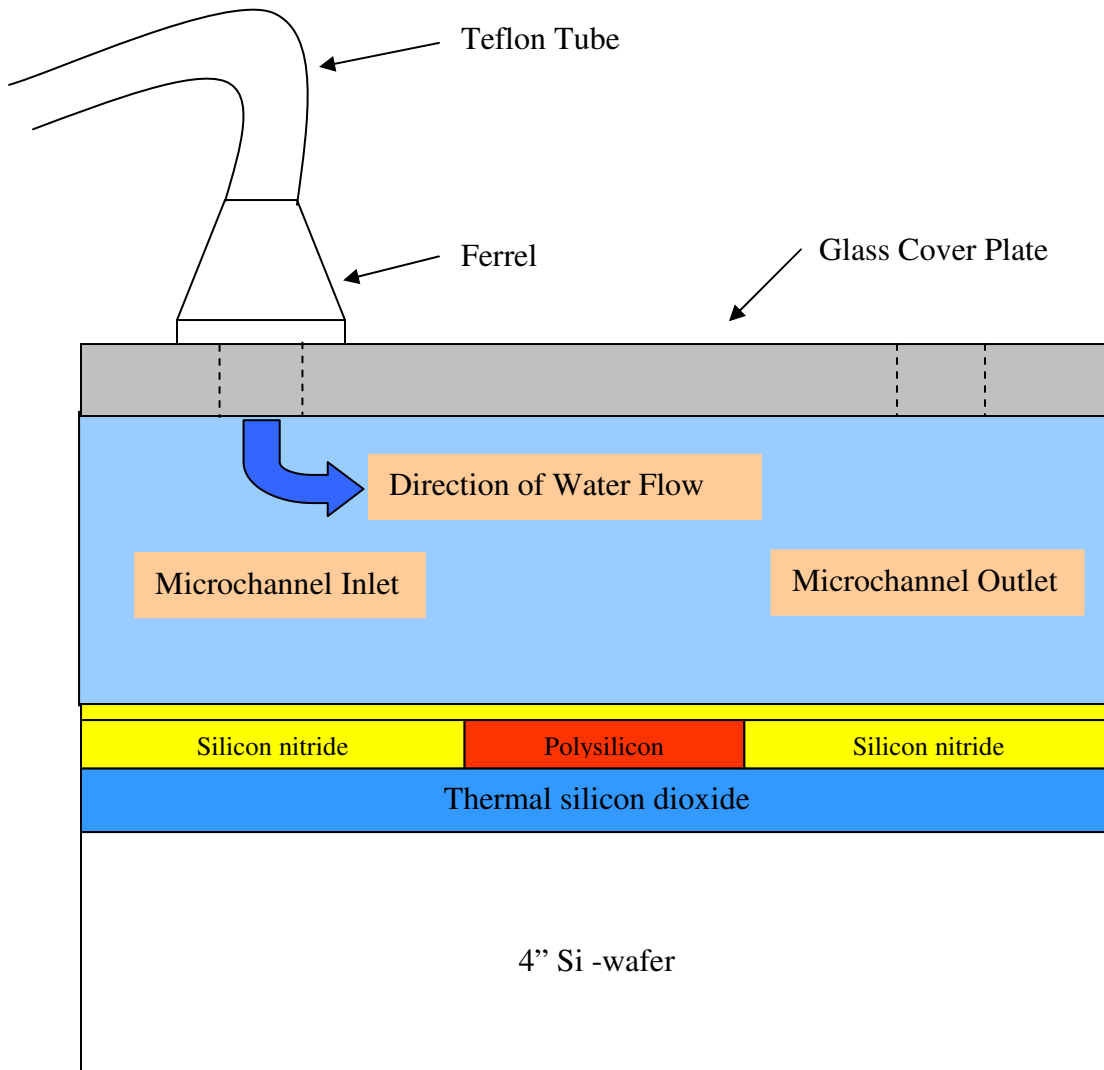
Figure 5-2 Schematic of the device with Teflon tube

The power to the sensor is supplied by a constant voltage power supply. The connection between the bonding pads and power supply is achieved by means of two probes. Figure 5-3 shows a device wafer held by means of a vacuum chuck. Contact probes shown are in contact with the bond pads (100 * 100 μm^2) on the wafer.
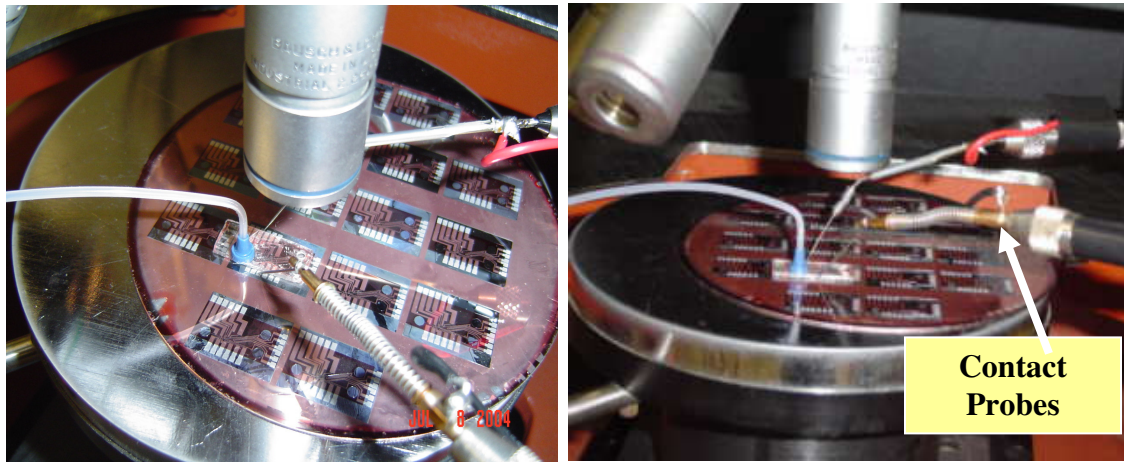
Figure 5-3 Device Wafer with Contact Probes

The glass plate was bonded to the chip by means of super glue (Chase Pitkin, NY). A ferrel (Flangeless fittings for 1/16" OD tubing www.upchurch.com) was bonded to the glass plate using super glue. While using super glue, the parts to be glued should be clean and dry. Glue should be applied one drop per square inch and parts should be pressed gently together for 10 seconds. The glued assembly should be allowed to set for a few minutes and then it should be ready. A Teflon tube (0.030" X 1/16" www.upchurch.com) was connected to the ferrel to facilitate water supply through the microchannel.

As shown in Figure 5-4, the power supply is used to supply voltage. A multimeter connected in series is used to measure the current flowing through the shear stress sensors.

Constant Voltage Supply

Water flow direction

Thermal hot film sensor
– Polysilicon resistor

A
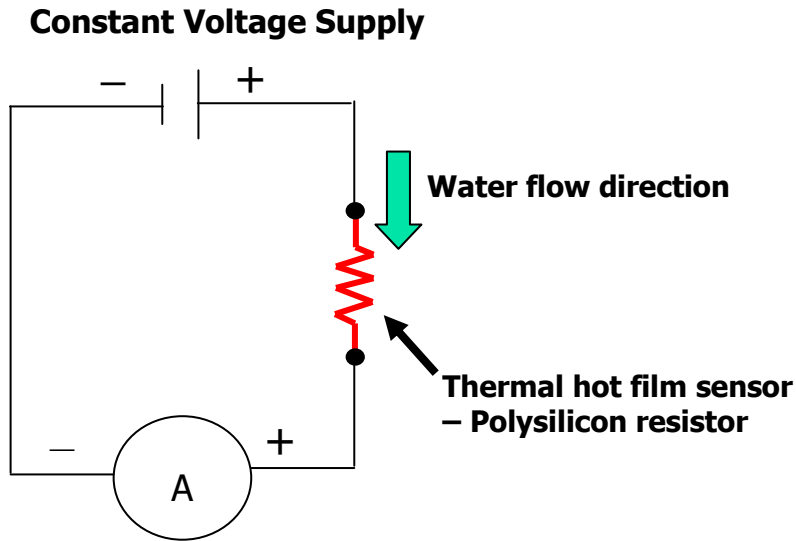
Figure 5-4 Schematic of Circuit

A 1 CC syringe as shown in Figure 5-5 was used to force water through the microchannel. A 0.1 CC water was forced manually for approximately 7.5 seconds using a 1 CC syringe to create a flow through microchannel. Therefore, Q = 0.1 CC / 7.5 sec = 0.8 CC / min = 48 CC / hr = 48 ml / hr. Thus, this flow rate was corresponding to Re ~ 1000 for a water flow through a microchannel of diameter 17 µm. Table 5-1 gives the data collected for various applied voltages.
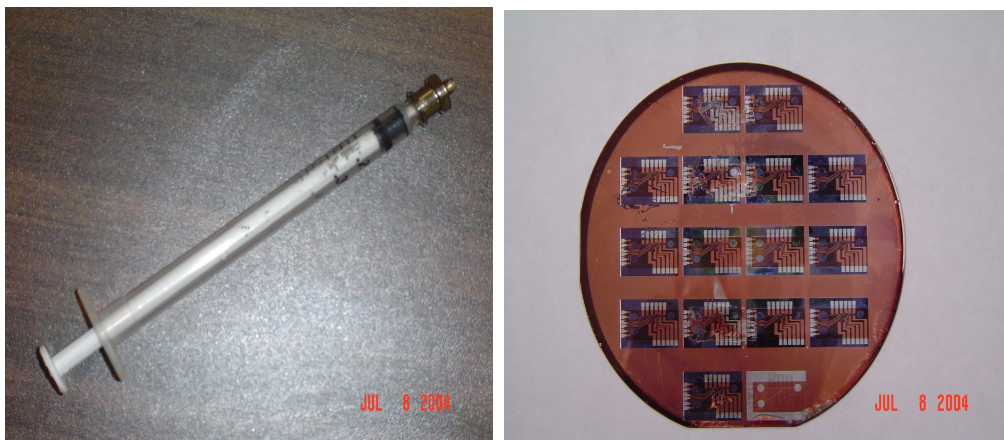
Figure 5-5 Syringe and Device Wafer

Table 5-1 Experimental Results

Trial	Voltage in V	Current at t = 0 sec in mA	Current during flow in mA	Current at t = 7.5 sec in mA
1	1.509	0.2032	0.2033	0.2033
2	1.509	0.2034	0.2039	0.2032
3	1.509	0.2030	Variable noise	0.2031
4	2.023	0.2724	Variable noise	0.2713
5	2.023	0.2720	Variable noise	0.2720
6	2.994	0.4048	Variable noise	0.4037
7	2.994	0.4027	0.4034	0.4024
8	2.994	0.4034	0.4044	0.4034
9	2.994	0.4039	Variable noise	Variable noise
10	1.483	0.1828	0.1830	0.1828
11	1.483	0.1828	0.1830	0.1829
12	1.483	0.1829	0.1830	0.1828
13	2.497	0.3085	0.3085	0.3084
14	2.497	0.3084	0.3084	0.3084
15	2.497	0.3083	0.3083	0.3083
16	1.484	0.1789	0.1789	0.1789
17	1.484	0.1789	0.1789	0.1789
18	2.064	0.2495	0.2495	0.2494
19	2.510	0.3038	0.3037	0.3038
20	2.510	0.3039	0.3039	0.3039
21	3.527	0.4284	0.4281	0.4284
22	3.527	0.4284	0.4278	0.4284
23	4.100	0.4985	0.4987	0.4987
24	4.100	0.4988	0.4988	0.4988
25	4.100	0.5044	0.5042	0.5041
26	5.050	0.6201	0.6198	0.6200
27	5.050	0.6204	0.6204	0.6204
28	1.011	0.1187	0.1186	0.1185
29	0.957	0.1260	0.1260	0.1260
30	1.526	0.2010	0.2013	0.2013
31	1.526	0.2010	0.2013	0.2010
32	1.526	0.2009	0.2010	0.2011
33	2.065	0.2719	0.2723	0.2719

Trial	Voltage in V	Current at t = 0 sec in mA	Current during flow in mA	Current at t = 7.5 sec in mA
34	2.065	0.2720	0.2720	0.2720
35	2.499	0.3293	0.3293	0.3293
36	3.020	0.3977	0.3970	0.3970
37	5.500	0.7229	0.7226	0.7228
38	5.990	0.7853	0.7854	0.7853
39	5.990	0.7852	0.7844	0.7841
40	6.000	0.7866	0.7862	0.7861
41	7.040	0.9199	0.9204	0.9192
42	7.030	0.9179	0.9173	0.9180
43	10.010	1.2874	1.2877	1.2874
44	10.010	1.2868	1.2851	1.2858
45	10.010	1.2864	1.2864	1.2864
46	10.010	1.2864	1.2874	1.2853
47	10.010	1.2852	1.2854	1.2852
48	10.010	1.2851	1.2856	1.2851
49	11.040	1.4007	1.4009	1.4007
50	11.040	1.4012	1.4012	1.4012
51	11.040	1.4012	1.4015	1.4012
52	11.040	1.4010	1.4012	1.4010
53	11.040	1.4009	1.4013	1.4012
54	11.040	1.4012	1.4014	1.4012

During the first few trials a considerable change in the current was observed during the flow. It was inferred that it was due to the noise present due to the long wiring between the sensor and the meters. Hence the shortest possible wiring scheme was used and it was observed that the noise was reduced to 1 μA. The sensors were tested for various voltages and the corresponding current was measured with and without water flow through microchannel (Table 5-1). Consider a trial # 31 in Table 5-1. Resistance of hot film sensor with no water flow = V / $I_{t=0}$ = 1.526 V/ 0.2030 mA = 7.517 KΩ. Similarly, resistance of hot film sensor with water flow (Re ~ 1000) = V / I $_{during\ flow}$ =

1.526 V / 0.2033 mA = 7.506 KΩ. Thus, during water flow, resistance of hot film sensor was dropped by 11 Ω. A drop in resistance implied a drop in temperature of hot film. Thus, it can be inferred that during the flow, heat was carried away by water which resulted in reduction of hot film temperature and hence the resistance. This verified the thermal -transfer principal of hot film shear stress sensors. Similar conclusion can be drawn for trial # 8, 33, 43, 48 and 51.

Since the heat loss to the substrate of the hot film are difficult to predict, the hot film sensors must be calibrated to determine A and B (Equation 2-26). The fabricated hot film sensor can be calibrated in order to determine the wall shear stress corresponding to various fluid velocities. The ratio between input power and temperature variation versus the shear stress to the 1/3 power can be plotted (Section 6.3 Figure 6-4) and calibration constants A and B can be determined for the hot film sensor. The following additional test set up will be needed in order to calibrate the sensor:

1. A constant temperature circuit to determine supply power to the sensor to keep it at a constant operating temperature of 310 K for a given fluid flow through microchannel. (Section 6.3 Figure 6-3)

2. A micro syringe pump to accurately measure flow rate through microchannel. (Section 6.3 Figure 6-2)

Thus, for any unknown fluid flow through microchannel, using equation 5-1, the wall shear stress can be determined.

$$\frac{I^2 R}{\Delta T} = A \left(\rho \tau_w \right)^{1/3} + B \tag{5-1}$$

Know quantities-

I^2R = Determined from CT circuit

$\Delta T = T_R - T_o = 310\ K - 300\ K = 10\ K$

A and B = Determined from a calibration curve

ρ = Density of water

Unknown quantity-

τ_w = Wall shear stress corresponding to a given fluid flow

5.2. Summary and Conclusions

A device was successfully tested using a manual syringe at SMFL, RIT. A super glue served as a good means for bonding the glass plate to AZ PLP resist and also ferrel to the glass plate. A 1CC syringe used created a water flow through microchannel. The current through hot film sensor was measured with and with out water flow through microchannel. The current measurements aided to verify thermal-transfer principle of hot film shear stress sensors.

Chapter 6

Future work

6.1. Device design

The length of the polysilicon resistors should be increased. It can be observed from Figure 6-1 that contact cuts are in the channel due to overlay errors during the device fabrication.
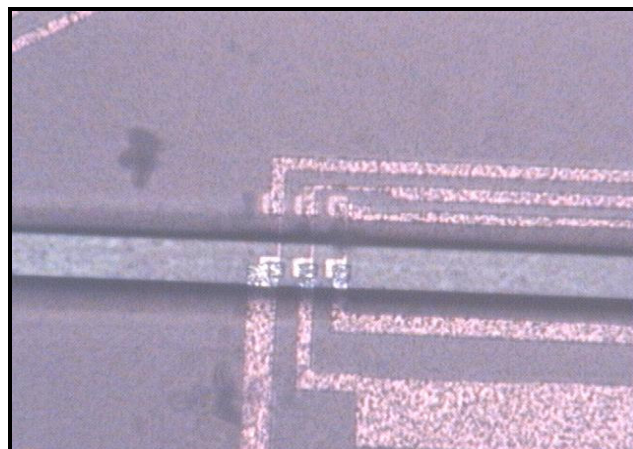

Figure 6-1 Misalignment – Sensor and Microchannel

This is undesirable because aluminum comes in contact with water. Upon applying a voltage > 3 V, aluminum corrodes once in contact with water. Increasing the length of the resistors will eliminate this problem. The size of the contact cuts should be increased to avoid misalignment due to overlay errors.

It is recommended to have alignment key at photo II level (Contact cuts) since the alignment key at photo I level (Polysilicon resistors) is not visible during photo III level (Metallization).

6.2. Device fabrication

It was planned to use SU-8 2015 negative photoresist to fabricate microchannels because of its good mechanical, thermal and chemical stability upon cure. SU-8 after expose and PEB is highly cross-linked epoxy, which makes it extremely difficult to remove with conventional solvent based resist strippers. The removal processes include immersion in oxidizing acids such as piranha etch/clean, plasma ash, RIE, laser ablation and pyrolisis. It was difficult to remove SU-8 upon misalignment (due to overlay errors) between resistors and microchannel. Thus, for the present work microchannels are fabricated in AZ – EXP PLP 100 XT positive photoresist. The resist is obtained from Clariant Corporation (www.azresist.com). Thicknesses of 50 µm can be obtained at 600 rpm and thicknesses of 15 µm can be obtained at 1500 rpm using a single coat process. It can be easily stripped off using acetone and hence recommended for future use.

6.3. Device Testing and Calibration

It is highly recommended to use a micro-syringe pump to create a flow in microchannel. The various flow rates can be used for the sensor calibration. A Genie syringe pump as shown in Figure 6-2 can be purchased from Kent Scientific Corporation (www.KentScientific.com).

Figure 6-2 Genie Syringe Pump (www.KentScientific.com)

This pump accepts very small to large syringes, up to 60 CC. Flow rates as low as 6 µl/hr or as high as 1200 ml/hr can be dispensed.

A constant temperature (CT) mode circuit (Temperature of the shear stress sensor remains constant during the operation) as shown in Figure 6-3 should be employed for the calibration of the sensor and to obtain calibration constants A and B.
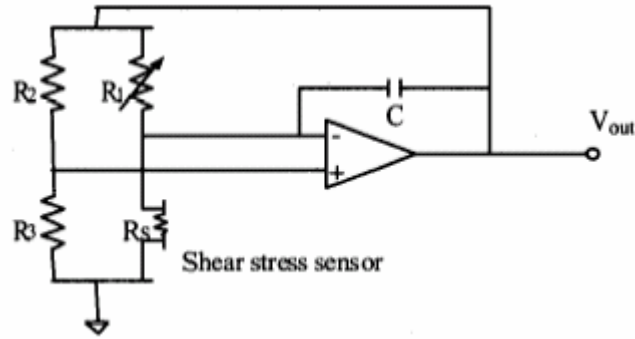
Figure 6-3 A simplified CT circuit (Yong Xu et. al 2000)

The CT circuit contains a feedback loop that keeps the voltage across the sensor resistor R_S constant. The sensor is a part of wheatstone bridge configuration. As shown in Figure 6-3, R_S is the shear stress sensor, R_1 is adjustable resistor, and a resistor R2 equals R_3. R_1, R_2 and R_3 should have nearly zero TCR. An important parameter for the operation of the shear stress sensor is the overheat ratio, α_R. It is defined as

$$\alpha_R = \frac{(R_S - R_{S0})}{R_{S0}} \tag{6-1}$$

where R_S is the resistance of the sensor at the operating temperature and R_{S0} is the resistance at the ambient temperature. More details about the CT circuit operation can be found in Gupta et. al 1996.

The hot film sensor can be calibrated and calibration constants A and B (Equation 2-26) can be determined by obtaining a plot of the ratio between input power and temperature variation versus the shear stress to the 1/3 power as shown in Figure 6-4. Figure 6-4 also shows lines for constant current mode and constant voltage mode (Liu, 1999) operations. The wall shear stress corresponding to various volumetric flow rates can be calculated as described in Section 3.3.1. The power, $P = I^2 R_{OP}$, to keep hot film

sensor to a constant temperature can be obtained from CT mode circuit for various flow rates. According to equation 2-26, the slope of the CT curve in Figure 6-4 corresponds to constant A and the intercept on Y axis is constant B. Thus, the hot film sensor can be calibrated.
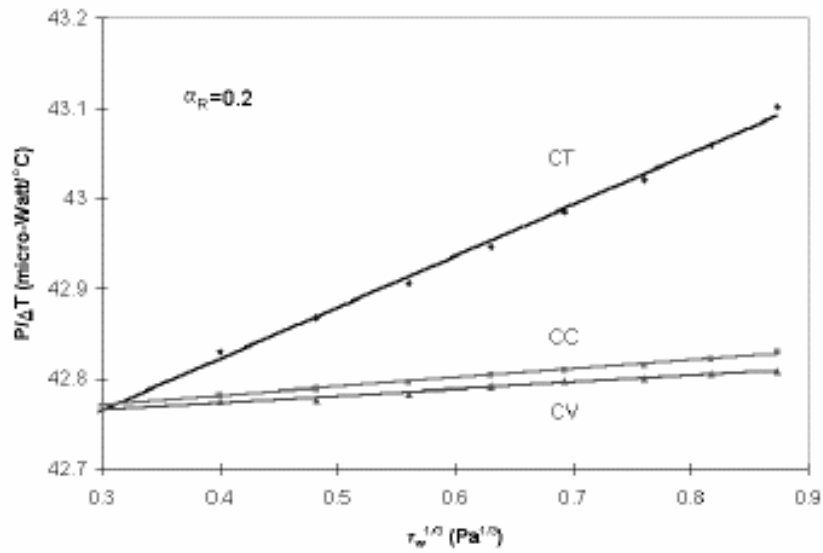

Figure 6-4 The ratio between input power and temperature variation versus the shear stress to 1/3 power (Liu, 1999)

Chapter 7
Conclusion

A micromachined hot film thermal shear stress sensor had been developed and successfully integrated with microchannel of size 17 * 17 µm^2 with bifurcation angle 30^0 at SMFL, RIT. CFD Fluent software served as a numerical tool to optimize the sensor dimensions and obtain the power requirements to the sensor. Surface micromachined used in the present work is the promising technology for the device fabrication. A working fluid, water was forced through the microchannels by means of a syringe and an attempt had been made to verify the thermal-transfer principle of hot film shear stress sensor. This thesis work was a first attempt to integrate the shear stress sensors with microchannels at RIT. After testing the sensors for various power inputs, it can be concluded that the suggestions made in section 6 should be incorporated for the next generation of the device for the successful calibration of the shear stress sensors and prediction of the wall shear stress along the microchannels.

References

Admiraal, D. M., Entrainment of Sediment by Unsteady Turbulent Flows, Ph.D. Thesis, University of Illinois at Urbana-Champaign, 1999.

Bellhouse, B. J. and D. L. Schultz, Determination of Mean and dynamic Skin Friction, Separation and Transition in Low-speed Flow with a Thin-film Heated Element, J. Fluid Mech., 24, 379-400, 1966.

Drolet, Y., Evaluation of Heated Film Sensors for the Measurement of Wall Shear Stress, MS Thesis, University of Toronto, 1992.

Fox and McDonald, Introduction to Fluid Mechanics, Fifth Edition, John Wiley and Sons, Inc., 1998.

Frame, M.D.S. and I. H. Sarelius, A System for Culture of Endothelial Cells in 20-50 µm Branching Tubes, Micorcirculation, vol. 2, No. 4 377-385, 1995.

Gottmann, M., Local Wall Shear Stress and Interface Behavior of Adiabatic Air-Water Flows in Rectangular Ducts, Ph.D. Thesis, University of Arizona, 1997.

Grande, W. J., Fabrication Technologies for Advanced Heat Transfer Application, First International Conference on Microchannels and Minichannels, ICMM2003-1023, April 21-23, 2003.

Gupta, V., Analog VLSI for Active Drag Reduction (Shear Stress Control), Ph.D. Thesis, California Institute of Technology, 1997.

Gupta, B., R. Goodman, F. Jiang, and Y.C. Tai, Analog VLSI System for Active Drag Reduction, IEEE J. Microelectromech. Syst., vol. 16, no. 5, pp. 53-59, 1996.

Hagen, K. D., Heat Transfer with Applications, Prentice Hall, 1999.

Hanratty, T. J. and J. A. Campbell, Fluid Mechanics Measurements, Measurement of wall shear stress (Chapter 11), 2nd Edition, R. J. Goldstein, (Washington DC: Taylor and Francis), 575-648, 1996.

Haritonidis, J. H., Advances in Fluid Mechanics Measurements, The measurements of wall shear stress, ed M Gad-el-Hak (Berlin:Springer), 229-261, 1989.

Huang, J. B., C. Ho, S. Tung, C. Liu, and Y. Tai, Micro thermal shear stress sensor with and without cavity underneath, IEEE Instrumentation and Measurement Technology Conference, 171-174, 1995.

Hyman, D. J., T. Pan, M. Mehregany, E. Reshotko, and B. Willis, Characterization of Microfabricated Shear Stress Sensors, ICIASF Record, International Congress on Instrumentation in Aerospace Simulation Facilities, 6.1-6.7, 1995.

Jiang, F., Silicon Micromachined Flow Sensors, Ph.D. Thesis, California Institute of Technology, 1996.

Jiang, F., Yu-Chong Tai, B. Gupta, R. Goodman, S. Tung, Jin-Biao Huang, and Chih-Ming Ho, A Surface-micromachined Shear Stress Imager, Micro Electro Mechanical Systems, 1996, MEMS '96, Proceedings. 'An Investigation of Micro Structures, Sensors, Actuators, Machines and Systems'. IEEE, The Ninth Annual International Workshop , 110 – 115, 11-15 Feb. 1996.

Jiang, F., Yong Xu, T. Weng, Z. Han, Y. Tai, A. Huang, C. Ho, and S. Newbern, Flexible Shear Stress Sensor Skin for Aerodynamics Applications, Micro Electro Mechanical Systems, 2000. MEMS 2000. The Thirteenth Annual International Conference on MEMS, 364–369, 23-27 Jan. 2000.

Jiang, F., Y. Xu, Q. Lin, J. Clendenen, and S. Tung, and Y. Tai, Underwater shear-stress sensor, Proceedings of the IEEE Micro Electro Mechanical Systems (MEMS), 340-343, 2002.

Kikuchi, Y., K. Sato, H. Ohki, and T. Kaneko, Optically Accessible Microchannels Formed in a Single-Crystal Silicon Substrate for Studies of Blood Rheology, Microvascular Reasearch, 44, 226-240, 1992.

Kikuchi, Y., Q. Da, and T. Fujino,Variation in Red Blood Cell Deformability and Possible Consequences for Oxygen Transport to Tissue, Microvascular Reasearch, 47, 222-231, 1994.

Kimura, M. S. Tung, J. Lew, C. M. Ho, F. Jiang, and Y. C. Tai, Measurements of wall shear stress of a turbulent boundary layer using a micro-shear-stress imaging chip, Fluid Dynamics Research, v 24, n 6, 329-342, Jun. 1999.

Lennart, Lofdahl and Mohamed Gad-el-Hak, MEMS-based pressure and shear stress sensors for turbulent flows, Meas. Sci. Technology, 10, 665-686, 1999.

Liu, C., Silicon Micromachined Sensors and Actuators for Fluid Mechanics Applications, Ph.D. Thesis, California Institute of Technology, 1996.

Liu, C., Jin-Biao Huang, Z. Zhu, F. Jiang, S. Tung, Yu-Chong Tai, and Chih-Ming Ho, A Micromachined Flow Shear-stress sensor based on Thermal Transfer Principles, Journal of Microelectromechanical Systems, , 8 , Issue: 1 , 90 – 99, March 1999.

Ludwieg, H., Ein Gerat zur messung der wandschubspannung turbulenter Reibungschichten, Ing. Arch., vol. 17, pp. 207-218, 1949 (Instrument for Measuring the Wall Shearing Stress of Turbulent Boundary Layers, NACA 7M 1284, 1950).

Madou, M. J., <u>Fundamentals of Microfabrication</u>, Chapter 4, Wet Bulk Micromachining, CRC Press, 1997.

Madou, M. J., <u>Fundamentals of Microfabrication</u>, Chapter 9, Surface Micromachining, CRC Press, 1997.

Minamitani, H., K. Tsukada, T. Kawamura, E. Sekizuka, and C. Oshio, Analysis of Elasticity and Deformability of Erythrocytes using Microchannel Flow System and Atomic Force Microscope, 1st Annual International IEEE-EMBS Special Topic Conference on Microtechnologies in Medicine and Biology, October 12-14, 68-71, 2000.

Mitchell, J. E. and T. J. Hanratty, A Study of Turbulence at a Wall Using an Electrochemical Wall-Stress Meter, J. Fluid Mech., 26, 199-221, 1966.

Nagaoka, Y. H.G. Alexander, W. Liu, H. Wayne, and C. M. Ho, Shear stress measurements on an airfoil surface using micro-machined sensors, JSME International Journal, Series B, v 40, n 2, 265-272, May 1997.

Nguyen and Wereley, <u>Fundamentals and Applications of Microfluidics</u>, MEMS series, Artech House Publishers, 2002.

Noren, D., M. D. S. Frame and H. Palmer, A Study of Fluid Flow through Arteriolar Bifurcations: Computational Predictions and *In Vivo* Comparison, MS thesis, University of Rochester, Rochester, NY, 1999.

Oudheusden, Van B.W., Silicon Flow Sensors, Control Theory and Applications, IEE Proceedings D [see also IEE Proceedings-Control Theory and Applications], 135, Issue:5, 373 – 380, July 1988.

Padmanabhan, A., Silicon Micromachined Sensors and Sensor Arrays for Shear Stress Measurements in Aerodynamic Flows, Ph. D. Thesis, MIT, 1997.

Pan, T., Microfabricated Shear Stress Sensors, Ph. D. Thesis, CWRU, 1996.

Pan, T., D. Hyman, E. Reshotko, and M. Mehregany, Microfabricated Shear Stress Sensors, Part 2: Testing and calibration, AIAA Journal, v 37, n 1, 73-78, Jan. 1999.

Robinson, R. J, L. Fuller, H. Palmer and M. D. S. Frame, Design and Analysis of a Shear Stress Sensor for Microcirculation Investigations, Proceedings of FEDSM'03 4TH ASME_JSME Joint Fluids Engineering Conference Honolulu, Hawaii, USA, July 6-11, 2003.

Roche, D., C. Richard, L. Eyraud, and C. Audoly, Piezoelectric bimorph bending sensor for shear-stress measurement in fluid flow, Sensors and actuators. A, Physical. 55, no. 2-3, 157-162, 1996.

Schmidt, M. A., S. D. Senturia, and A.C. Smith, Micro sensors for the Measurement of Shear Forces in Turbulent Boundary Layers, Ph.D. Thesis, MIT, 1988.

Tracey, M., N. Sutton, I. Johnston, and W. Doetzel, A Microfluidics-Based Instrument for Cytomechanical Studies of Blood, 1st Annual International IEEE-EMBS Special Topic Conference on Microtechnologies in Medicine and Biology, October 12-14, 62-67, 2000.

Trimmer, W.S.N., Microrobots and Micromechanical Systems, Sensors and Actuators, 19, 267, 1989.

Walburn, F. J. and D. J. Schneck, A Constitutive Equation for Whole Human Blood, Biotechnology, 13, 201-210, 1976.

Wesley, C., D. Trebotich and D. Liepmann, Modeling of Blood Flow in Simple Microchannels, Modeling and Simulation of Microsystems, ISBN 0-9708275-0-4, 218-222, 2001.

William, P. E. and J. H. Smith, Micromachined Pressure Sensors: Review and Recent Developments, SPIE , 3046, 30-41, 1997.

www.fluent.com.

www.Kentscientific.com.

Xu, Y., Chen-Wei Chiu, F. Jiang, Q. Lin, and Yu-Chong Tai, Mass Flowmeter using a Multi-sensor Chip, Micro Electro Mechanical Systems, 2000. MEMS 2000. The Thirteenth Annual International Conference on MEMS, 541-546, 23-27 Jan. 2000.